

Distinguishing Kerr naked singularities and black holes using the spin precession of a test gyro in strong gravitational fields

Chandrachur Chakraborty^{1,*} Mandar Patil^{2,†} Prashant Kocherlakota^{1,‡}

Sudip Bhattacharyya^{1,§} Pankaj S. Joshi^{1,¶} and Andrzej Królak^{2,**}

¹*Tata Institute of Fundamental Research, Mumbai 400005, India and*

²*Institute of Mathematics of Polish Academy of Sciences, Śniadeckich 8, 00-956 Warsaw, Poland*

We consider here the precession of a test gyroscope in Kerr spacetimes to distinguish a naked singularity (NS) from black hole (BH). It is known that when the angular velocity of the gyro vanishes the spin precession frequency diverged at the ergo-surface. We show that it is possible to overcome this divergence by moving the gyro to the ergoregion with a non-zero angular velocity (Ω_e) in a definite range. Then the frequency is finite and regular on the boundary of the ergoregion and inside, for both the BH and NS. Specifically, if we move the gyro with a non-zero Ω_e to an unknown astrophysical object, its precession diverges on the event horizon for a black hole, but finite and regular for NS. Therefore a genuine detection for the existence or otherwise of the event horizon becomes possible. We also show that for a near-extremal ($1 < a_* < 1.1$) NS, some special features appear in precession frequency curves, using which a near-extremal NS can be distinguished from a BH, or NS with higher angular momentum. We then investigate the Lense-Thirring (LT) precession or nodal plane precession frequency, and other fundamental frequencies, for the accretion disk around a BH and NS to show that clear distinctions exist for BH and NS configurations in terms of radial variation features. The LT precession in equatorial circular orbits increases closer to BH, but for NS it increases, attains a peak and then decreases. Specifically, for $a_* = 1.089$, it decreases to reach 0 for certain r_0 , and acquires negative values for $a_* > 1.089$. For $1 < a_* < 1.089$, a peak appears, but vanishing or negative LT frequency are avoided. Hence there are important differences in accretion disk LT frequencies for BH and NS. As LT frequencies are intimately related to and can cause the observed QPOs, this may allow to determine whether a given astrophysical object is BH or NS.

* chandrachur.chakraborty@tifr.res.in

† mpatil@impan.pl

‡ k.prashant@tifr.res.in

§ sudip@tifr.res.in

¶ psj@tifr.res.in

** krolak@impan.pl

I. INTRODUCTION

An important issue in relativistic astrophysics and gravitation theory today has been to rule out the existence of NSs in gravitational collapse of massive matter clouds. Alternatively, if NSs do exist, even in theory, as endstates of massive stars collapsing under self-gravity towards the end of their life-cycles, the important physical question would then be, how can one decide whether a particular astrophysical compact object is a BH or a NS. This is a key issue, really at the heart of making physical predictions about very strong gravity regions in the universe, which major astrophysical missions are probing currently [1].

In this connection, it is important to examine, in some detail, the Kerr geometry configurations and find physical quantities that can be used to differentiate BH from NS. The Kerr spacetime describes either a rotating black hole or a naked singularity, based on the Kerr spin parameter a , which is the specific angular momentum (J/M). Every compact rotating object has an ergosphere or an ergoregion located outside it. This region derives its name from the Greek word ‘ergon,’ which means ‘work,’ to indicate that it is possible to extract energy from this region. The ergosphere has an oblate spheroidal shape and touches the event horizon at the pole. As one moves from the pole to equator, the radius of this region increases and reaches its maximum. In general, a BH possesses two event horizons and two ergoregions which are the outer and inner event horizons and outer and inner ergoregions. The region between the outer event horizon and outer ergoradius is called the outer ergoregion or simply the ergoregion. In this paper, we will be primarily concerned with this region. Similarly, the region between the inner event horizon and the inner ergoregion is called the inner ergoregion. The inner ergoregion is often dismissed as being unphysical since we don’t really know reliably what happens behind the outer event horizon of a rotating BH. The rotational energy of the BH can be extracted by a particle from the outer ergoregion (henceforth, just ergoregion) and this is called Penrose process. The ergoregion is responsible for several interesting phenomena. One of these has been recently discussed in Ref.[2] where the exact Lense-Thirring (LT) precession frequency of a test gyroscope in Kerr spacetime has been derived and shown that the LT precession frequency diverges on the boundary of the ergoregion (henceforth, ‘ergosurface’) of a BH (dimensionless Kerr parameter $a_* = J/M^2 \leq 1$). In another work [3], the spin precession frequency has been discussed in detail in the case of NS ($a_* > 1$). In the case of the NS, the region between the inner and outer ergo radii is defined to be the ergoregion. It has been discussed there that the drastic change in geometry of the ergoregion for $a_* > 1$, as opposed to $a_* \leq 1$, could allow for a differentiation of the two space-times using a physical quantity, which in this case was the precession frequency of gyroscopes placed around these compact objects. Specifically, for the NS

configuration, along the pole a finite angle opens up where the ergoregion is absent and $r = 0$ can be accessible via this region without passing through the ergoregion. This region broadens with increasing the value of a_* beyond 1 and the ergoregion shrinks toward the equator. It was discussed that the precession frequency always diverges on the ergosurface. Since the ergoregion completely bounds a BH, on ‘approaching’ it in any direction, one would find a divergence. Whereas, in the case of a NS, the frequency remains finite and regular in the ‘opening angle’ due to the absence of the ergoregion. We find this to be a possible experiment to distinguish the two qualitatively distinct Kerr configurations.

Previously, it has been discussed in Ref.[4] how a non-rotating black hole can be distinguished from a naked singularity. In this article, we discuss how one can distinguish a BH from a NS using the behavior of the precession frequency of the spin of a test gyro which moves along a non-geodesic orbit around such a Kerr compact object. In this regard, we find it useful to mention that recently Bini et al. have analyzed the precession of a test gyroscope along bound [5] and unbound [6] equatorial plane geodesic orbits around a BH with respect to a static reference frame whose axes point towards ‘fixed stars.’ It is well known that the paths followed by spinning test particles are not, in general, geodesics [7, 8]. In our present article, we discuss the precession of a gyroscope both outside and inside the ergoregion of a BH and NS. We find that the divergence of the spin precession frequency on the ergosurface reported in Ref.[3] can be avoided if the test gyro moves with a non-zero angular velocity Ω_e . In Ref.[3], the motivation was to study the precession of spins of gyroscopes attached to stationary observers, that is, to answer physical questions like ‘how will the gyroscope of an astronaut holding his spaceship at a constant distance from a Kerr compact object behave?’ The four-velocity (u) of ‘stationary gyros’ on the ergosurface satisfies $u.u = 0$, that is, it becomes null. However, if one introduces an azimuthal component to the four-velocity, the norm can be made non-zero and also time-like. Now, we can describe the behavior of a gyro inside the ergoregion. We find that the precession frequency of the gyro behaves differently inside the ergoregion of a BH versus that of a NS, due to the presence of the event horizon, therefore rendering it a viable physical quantity that can be used to distinguish a BH from a NS.

Later, we examine and investigate the Lense-Thirring precession frequency and the fundamental frequencies of an accretion disk around a Kerr compact object. Stable circular orbits in the equatorial plane for both the BH and NS cases are investigated, and we show that there are important characteristic differences which can be used to distinguish the BH and NS configurations from each other.

Specifically, we find that the features of stable circular orbits in the equatorial plane for both the BH and NS cases are noted. We also show here that the radial and epicyclic frequencies show rather

distinct features in the BH and NS cases. Further, in observed QPOs from accretion disks, if one finds a clear peak at some radius, then the existence of NSs could possibly be established.

II. STATIONARY OBSERVERS IN KERR SPACETIME

Observers can remain stationary in a rotating spacetime with respect to infinity, only outside the ergoregion. Once inside, it is impossible to remain stationary without changing all three spatial coordinates (say, r, θ, ϕ) of their world lines with time. Using large amounts of rocket power or some other source of thrust, an observer can hover very close to the horizon of a Schwarzschild BH. However, this is not possible in the case of a BH since its event horizon lies inside its ergosphere. However, it is possible to remain fixed at a particular r and θ by rotating with respect to infinity. Thus, the four-velocity of a stationary observer inside the ergoregion can be expressed as

$$u = u_{\text{obs}}^\alpha = u_{\text{obs}}^t (1, 0, 0, \Omega_e) \quad (1)$$

where t is the time coordinate and Ω_e is the angular velocity of the observer. Ω_e has a certain range for which the above velocity describes a time-like observer inside the ergoregion. The range of Ω_e can be determined using the condition that u should be timelike at each point (r, θ) of the ergoregion. Outside the ergosphere, an observer can remain stationary, with zero angular velocity, and their four-velocity given as

$$u_{\text{obs}}^\alpha = u_{\text{obs}}^t (1, 0, 0, 0). \quad (2)$$

Also, an observer outside the ergoregion can have any angular velocity, that is they can take the form of the velocity mentioned in Eq.(1) with no restriction on Ω_e .

III. SPIN PRECESSION OF A TEST GYROSCOPE : FORMALISM

The spin precession frequency of a test gyro in any stationary spacetime can be expressed in the notation of Ref. [9] as

$$\tilde{\Omega} = \frac{1}{2K^2} * (\tilde{K} \wedge d\tilde{K}) \quad (3)$$

where K is the timelike Killing vector field and Ω is the spin precession frequency in coordinate basis. \tilde{K} and $\tilde{\Omega}$ are the one-forms of K and Ω respectively and $*$ represents the Hodge star operator or Hodge

dual. In any stationary spacetime, K can be chosen to be $K = \partial_0$ for which Eq.(3) becomes the Lense-Thirring (LT) precession frequency (Ω_{LT}). This can be expressed as [2, 9],

$$\Omega_{\text{LT}} = \frac{1}{2} \frac{\varepsilon_{ijl}}{\sqrt{-g}} \left[g_{0i,j} \left(\partial_l - \frac{g_{0l}}{g_{00}} \partial_0 \right) - \frac{g_{0i}}{g_{00}} g_{00,j} \partial_l \right]. \quad (4)$$

In a static spacetime, LT precession vanishes since $g_{0i} = 0$. On the other hand, it does not vanish in a stationary spacetime. Moreover, due to the presence of $K^2 = g_{00}$ in the denominator, Eq.(3) and Eq.(4) diverge if g_{00} vanishes. In a stationary and axisymmetric spacetime, this happens only on the ergosurface, which makes K a null vector there. Inside the ergoregion, K is no longer timelike but becomes spacelike. Thus, Eq.(4) is invalid inside the ergoregion as well as on its boundary.

To find how precession behavior is modified on entering the ergoregion, one can introduce an azimuthal component to the four-velocity, as mentioned in Sec.II and choose $K = K_e$ inside the ergoregion for which K_e^2 is non-zero on the ergosurface, that is we can choose K_e such that it is timelike on and inside the ergosurface. We can write this timelike Killing vector K_e inside the ergoregion as:

$$K_e = \partial_0 + \Omega_e \partial_c. \quad (5)$$

where ∂_c is a spacelike Killing vector in that stationary and axisymmetric spacetime. This means that this particular spacetime is independent of x^0 and x^c coordinates. Therefore, the corresponding co-vector of K_e can be written as

$$\tilde{K}_e = g_{0\nu} dx^\nu + \Omega_e g_{\gamma c} dx^\gamma \quad (6)$$

where $\gamma, \nu = 0, c, 2, 3$ in 4-dimensional spacetime. Separating space and time components we can write \tilde{K}_e as

$$\tilde{K}_e = (g_{00} dx^0 + g_{0c} dx^c + g_{0i} dx^i) + \Omega_e (g_{0c} dx^0 + g_{cc} dx^c + g_{ic} dx^i) \quad (7)$$

where $i = 2, 3$. Since we are mainly interested in the ergoregion of a stationary and axisymmetric spacetime, we can abolish g_{0i} and g_{ic} terms. Finally, we obtain

$$\tilde{K}_e = (g_{00} dx^0 + g_{0c} dx^c) + \Omega_e (g_{0c} dx^0 + g_{cc} dx^c) \quad (8)$$

and

$$d\tilde{K}_e = (g_{00,k} dx^k \wedge dx^0 + g_{0c,k} dx^k \wedge dx^c) + \Omega_e (g_{0c,k} dx^k \wedge dx^0 + g_{cc,k} dx^k \wedge dx^c). \quad (9)$$

Now, Eq.(3) can be modified as

$$\tilde{\Omega}_p = \frac{1}{2K_e^2} * (\tilde{K}_e \wedge d\tilde{K}_e). \quad (10)$$

Substituting the expressions of \tilde{K}_e and $d\tilde{K}_e$ in Eq.(10), we obtain the one-form of the precession frequency¹ as:

$$\tilde{\Omega}_p = \frac{\varepsilon_{ckl} g_{l\mu} dx^\mu}{2\sqrt{-g} \left(1 + 2\Omega_e \frac{g_{0c}}{g_{00}} + \Omega_e^2 \frac{g_{cc}}{g_{00}} \right)} \left[\left(g_{0c,k} - \frac{g_{0c}}{g_{00}} g_{00,k} \right) + \Omega_e \left(g_{cc,k} - \frac{g_{cc}}{g_{00}} g_{00,k} \right) + \Omega_e^2 \left(\frac{g_{0c}}{g_{00}} g_{cc,k} - \frac{g_{cc}}{g_{00}} g_{0c,k} \right) \right] \quad (11)$$

where we have used $\ast(dx^0 \wedge dx^k \wedge dx^c) = \eta^{0kcl} g_{l\mu} dx^\mu = -\frac{1}{\sqrt{-g}} \varepsilon_{kcl} g_{l\mu} dx^\mu$ and $K_e^2 = g_{00} + 2\Omega_e g_{0c} + \Omega_e^2 g_{cc}$.

Corresponding vector (Ω_p) of the co-vector $\tilde{\Omega}_p$ is

$$\Omega_p = \frac{\varepsilon_{ckl}}{2\sqrt{-g} \left(1 + 2\Omega_e \frac{g_{0c}}{g_{00}} + \Omega_e^2 \frac{g_{cc}}{g_{00}} \right)} \left[\left(g_{0c,k} - \frac{g_{0c}}{g_{00}} g_{00,k} \right) + \Omega_e \left(g_{cc,k} - \frac{g_{cc}}{g_{00}} g_{00,k} \right) + \Omega_e^2 \left(\frac{g_{0c}}{g_{00}} g_{cc,k} - \frac{g_{cc}}{g_{00}} g_{0c,k} \right) \right] \partial_l. \quad (12)$$

In a stationary and axisymmetric spacetime with coordinates $0, r, \theta, \phi$, Eq.(12) reduces to

$$\Omega_p = \frac{1}{2\sqrt{-g} \left(1 + 2\Omega_e \frac{g_{0\phi}}{g_{00}} + \Omega_e^2 \frac{g_{\phi\phi}}{g_{00}} \right)} \left[\left[\left(g_{0\phi,r} - \frac{g_{0\phi}}{g_{00}} g_{00,r} \right) + \Omega_e \left(g_{\phi\phi,r} - \frac{g_{\phi\phi}}{g_{00}} g_{00,r} \right) + \Omega_e^2 \left(\frac{g_{0\phi}}{g_{00}} g_{\phi\phi,r} - \frac{g_{\phi\phi}}{g_{00}} g_{0\phi,r} \right) \right] \partial_\theta - \left[\left(g_{0\phi,\theta} - \frac{g_{0\phi}}{g_{00}} g_{00,\theta} \right) + \Omega_e \left(g_{\phi\phi,\theta} - \frac{g_{\phi\phi}}{g_{00}} g_{00,\theta} \right) + \Omega_e^2 \left(\frac{g_{0\phi}}{g_{00}} g_{\phi\phi,\theta} - \frac{g_{\phi\phi}}{g_{00}} g_{0\phi,\theta} \right) \right] \partial_r \right]. \quad (13)$$

In polar coordinates, we can write the expression as

$$\vec{\Omega}_p = \frac{1}{2\sqrt{-g} \left(1 + 2\Omega_e \frac{g_{0\phi}}{g_{00}} + \Omega_e^2 \frac{g_{\phi\phi}}{g_{00}} \right)} \left[-\sqrt{g_{rr}} \left[\left(g_{0\phi,\theta} - \frac{g_{0\phi}}{g_{00}} g_{00,\theta} \right) + \Omega_e \left(g_{\phi\phi,\theta} - \frac{g_{\phi\phi}}{g_{00}} g_{00,\theta} \right) + \Omega_e^2 \left(\frac{g_{0\phi}}{g_{00}} g_{\phi\phi,\theta} - \frac{g_{\phi\phi}}{g_{00}} g_{0\phi,\theta} \right) \right] \hat{r} + \sqrt{g_{\theta\theta}} \left[\left(g_{0\phi,r} - \frac{g_{0\phi}}{g_{00}} g_{00,r} \right) + \Omega_e \left(g_{\phi\phi,r} - \frac{g_{\phi\phi}}{g_{00}} g_{00,r} \right) + \Omega_e^2 \left(\frac{g_{0\phi}}{g_{00}} g_{\phi\phi,r} - \frac{g_{\phi\phi}}{g_{00}} g_{0\phi,r} \right) \right] \hat{\theta} \right]. \quad (14)$$

For $\Omega_e = 0$, Eq.(14) reduces to

$$\vec{\Omega}_p|_{\Omega_e=0} = \frac{1}{2\sqrt{-g}} \left[-\sqrt{g_{rr}} \left(g_{0\phi,\theta} - \frac{g_{0\phi}}{g_{00}} g_{00,\theta} \right) \hat{r} + \sqrt{g_{\theta\theta}} \left(g_{0\phi,r} - \frac{g_{0\phi}}{g_{00}} g_{00,r} \right) \hat{\theta} \right] \quad (15)$$

which is applicable to outside of the ergoregion to obtain the LT precession frequency of a test gyro due to the rotation of any stationary and axisymmetric spacetime [10].

¹ Ω_p is not the LT precession frequency of the gyro. Since the gyro has a non-zero angular velocity Ω_e , the precession frequency Ω_p is modified. If we set $\Omega_e = 0$, we have $\Omega_p = \Omega_{LT}$. In this work, the expression of Ω_p describes the overall precession which includes the LT effect as well as some other effects (for eg., geodetic precession) which we will discuss as we proceed.

A. Application to Kerr Spacetime

Now, we can apply the above formalism to the Kerr spacetime to describe the behavior of a test gyro inside the ergoregion as well as the outside of it. The Kerr metric in Boyer-Lindquist coordinates can be written as

$$ds^2 = - \left(1 - \frac{2Mr}{\rho^2}\right) dt^2 - \frac{4Mar \sin^2 \theta}{\rho^2} d\phi dt + \frac{\rho^2}{\Delta} dr^2 + \rho^2 d\theta^2 + \left(r^2 + a^2 + \frac{2Mra^2 \sin^2 \theta}{\rho^2}\right) \sin^2 \theta d\phi^2 \quad (16)$$

where a is the Kerr parameter, defined as $a = J/M$. It measures the angular momentum per unit mass of the central object and,

$$\rho^2 = r^2 + a^2 \cos^2 \theta, \quad \Delta = r^2 - 2Mr + a^2. \quad (17)$$

For convenience, we define the dimensionless Kerr parameter $a_* = a/M = J/M^2$, which we shall use almost exclusively. The various metric components can be read off from Eq. (16). Likewise,

$$\sqrt{-g} = \rho^2 \sin \theta \quad (18)$$

Now, substituting the metric components of Kerr spacetime in Eq.(14), we obtain the spin precession rate of the gyro as

$$\vec{\Omega}_p = \frac{A \sqrt{\Delta} \cos \theta \hat{r} + B \sin \theta \hat{\theta}}{\rho^3 [(\rho^2 - 2Mr) + 4\Omega_e Mar \sin^2 \theta - \Omega_e^2 \sin^2 \theta [\rho^2(r^2 + a^2) + 2Ma^2 r \sin^2 \theta]]} \quad (19)$$

where,

$$\begin{aligned} A &= 2aMr - \frac{\Omega_e}{8} [8r^4 + 8a^2 r^2 + 16a^2 Mr + 3a^4 + 4a^2(2\Delta - a^2) \cos 2\theta + a^4 \cos 4\theta] + 2\Omega_e^2 a^3 Mr \sin^4 \theta, \\ B &= aM(r^2 - a^2 \cos^2 \theta) + \Omega_e [a^4 r \cos^4 \theta + r^2(r^3 - 3Mr^2 - a^2 M(1 + \sin^2 \theta)) \\ &\quad + a^2 \cos^2 \theta(2r^3 - Mr^2 + a^2 M(1 + \sin^2 \theta))] + \Omega_e^2 aM \sin^2 \theta [r^2(3r^2 + a^2) + a^2 \cos^2 \theta(r^2 - a^2)]. \end{aligned} \quad (20)$$

B. Range of Ω_e

We have already stated that we can apply Eq.(19) both inside and outside of the ergoregion. Outside of the ergoregion Ω_e can take *any* value (with the additional requirement : u should always be timelike for it) but Ω_e cannot take an arbitrary value inside the ergoregion. We can calculate the range of Ω_e by requiring that K_e be timelike inside the ergoregion and hence, its norm be negative,

$$K_e^2 = g_{\phi\phi} \Omega_e^2 + 2g_{t\phi} \Omega_e + g_{tt} < 0 \quad (21)$$

Therefore, the allowed values of Ω_e at any point inside the ergoregion are,

$$\Omega_-(r, \theta) < \Omega_e(r, \theta) < \Omega_+(r, \theta) \quad (22)$$

with,

$$\Omega_{\pm} = \frac{-g_{t\phi} \pm \sqrt{g_{t\phi}^2 - g_{\phi\phi}g_{tt}}}{g_{\phi\phi}}. \quad (23)$$

In the Kerr spacetime,

$$\Omega_{\pm} = \frac{2Mar \sin \theta \pm \rho^2 \sqrt{\Delta}}{\sin \theta [\rho^2(r^2 + a^2) + 2Ma^2 r \sin^2 \theta]} \quad (24)$$

which shows that the range of allowed values for Ω_e becomes increasingly limited as the observer is located closer and closer to the horizon (located at $r = r_+$) and is eventually limited to the single value

$$\Omega_H = \frac{a}{2Mr_+} \quad (25)$$

at the horizon of the BH. This is true even in the equatorial plane. In the equatorial plane, that is for $\theta = \pi/2$, Eq.(24) becomes

$$\Omega_{\pm}|_{\theta=\pi/2} = \frac{2Ma \pm r\sqrt{\Delta}}{r(r^2 + a^2) + 2Ma^2}. \quad (26)$$

We can see from Panel (a) of FIG.1 that $\Omega_+|_{\theta=\pi/2}$ and $\Omega_-|_{\theta=\pi/2}$ matches at $r \rightarrow r_+$ in the case of BH and the value of Ω_e becomes $\Omega_H \approx 0.31$ for $a_* = 0.9$. Panel (b) of the same figure shows that a small gap appears between the two curves at $r \approx M$ in case of the near-extremal NS with $a_* = 1.001$ and the two curves match with one another at $r \rightarrow 0$ with the value of $\Omega_e = 1/a_*$. In the case of NS with higher angular momentum, say, for $a_* = 2$ (see Panel (c)), the small gap disappears but the two curves match at $r \rightarrow 0$ as well.

To compare the behavior of the gyro inside the ergoregion of a BH and a NS, one can now plot $\Omega_p = |\vec{\Omega}_p|$ (the modulus of Eq.(19)) with r for different angles. For this, a suitable value of Ω_e must be chosen. For this purpose, we introduce the parameter q to scan the range of allowed values for Ω_e as follows,

$$\Omega_e = q \Omega_+ + (1 - q) \Omega_- = \frac{2Mar \sin \theta + (2q - 1) \rho^2 \sqrt{\Delta}}{\sin \theta [\rho^2(r^2 + a^2) + 2Ma^2 r \sin^2 \theta]} \quad (27)$$

where $0 < q < 1$. In principle, the values of q between 0 and 1 covers the whole range of Ω_e from Ω_+ to Ω_- . For an example, one can choose a characteristic value - the median of Ω_+ and Ω_- for Ω_e as,

$$\Omega_e = \frac{\Omega_+ + \Omega_-}{2} = \frac{2Mar}{\rho^2(r^2 + a^2) + 2Ma^2 r \sin^2 \theta}. \quad (28)$$

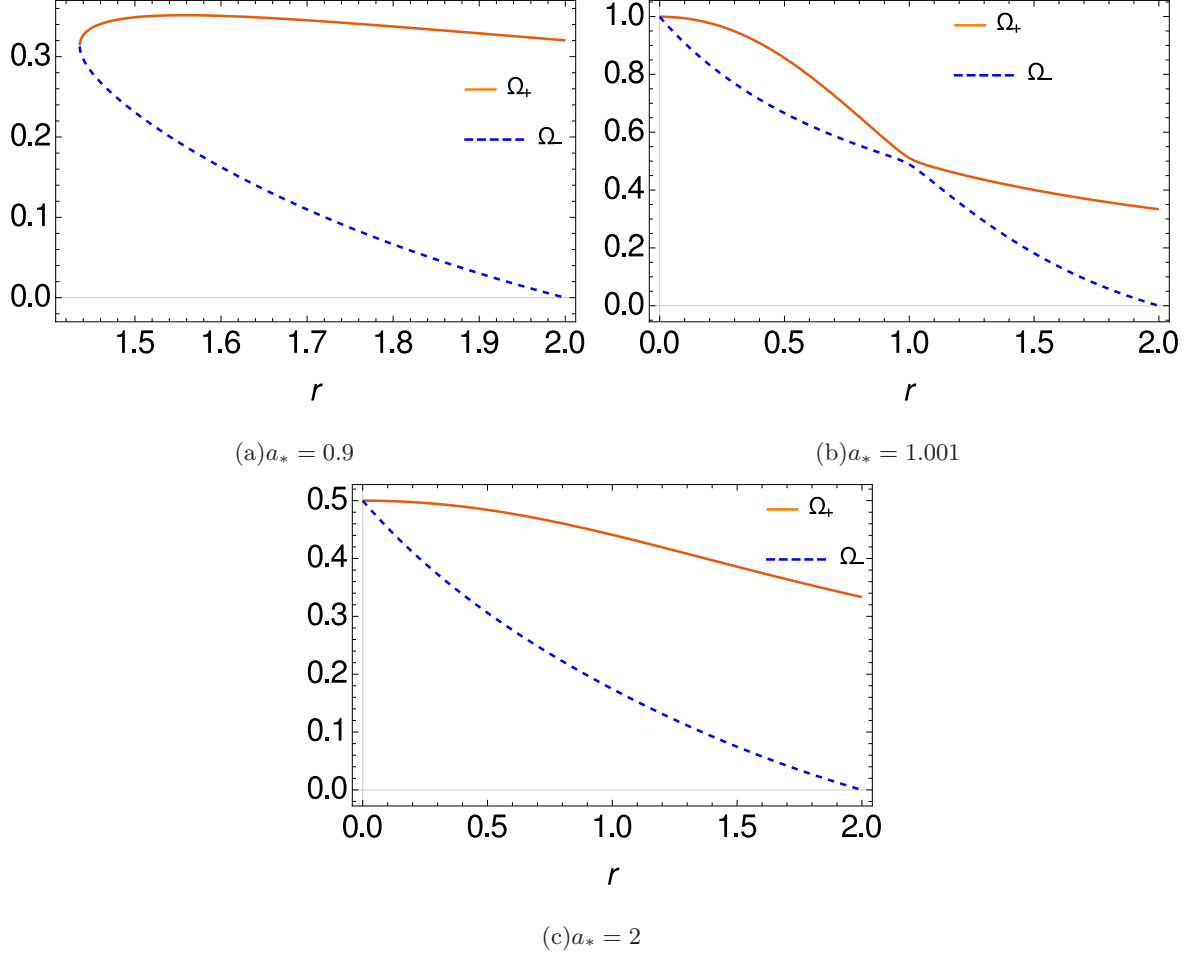


FIG. 1. Here we plot the boundary of the allowed range of Ω_e (in the unit of M^{-1}) of a gyroscope inside the ergoregion at the equatorial plane (using Eq.(26)) as a function of r (in the unit of M) for different values of Kerr parameter a_* . Gyro can take any value in the range : $\Omega_- < \Omega_e < \Omega_+$ inside the ergoregion.

Now, using expression Ω_e (Eq.(27)) we can simplify the denominator of Eq.(19) and obtain the final expression of spin precession frequency of a test gyro which is expressed as

$$\vec{\Omega}_p = \frac{\rho^2(r^2 + a^2) + 2Ma^2r \sin^2 \theta}{\rho^7 \Delta [1 - (1 - 2q)^2]} \cdot \left[A \sqrt{\Delta} \cos \theta \hat{r} + B \sin \theta \hat{\theta} \right] \quad (29)$$

where $0 < q < 1$ and A and B can be extracted from Eq.(20).

IV. SPECIAL CASES

A. Behavior of gyro frequency at $r = 0$

For NS, the region $r = 0$ is approachable from all directions except the equator, that is, $0 \leq \theta < 90^\circ$ and we can study the behavior of the precession frequency of a test gyro in this region. At $r = 0$, Eq.(19) becomes

$$\vec{\Omega}_p|_{r=0} = \frac{-a^2\Omega_e[3 + 4\cos 2\theta + \cos 4\theta]\hat{r} - 4M\sin 2\theta[1 - a\Omega_e(1 + \sin^2\theta) + a^2\Omega_e^2\sin^2\theta]\hat{\theta}}{8a^2\cos^4\theta[1 - a^2\Omega_e^2\sin^2\theta]} \quad (30)$$

since Eq.(20) becomes

$$\begin{aligned} A|_{r=0} &= -\frac{a^4\Omega_e}{8} [3 + 4\cos 2\theta + \cos 4\theta], \\ B|_{r=0} &= -Ma^3\cos^2\theta [1 - a\Omega_e(1 + \sin^2\theta) + a^2\Omega_e^2\sin^2\theta]. \end{aligned} \quad (31)$$

where the range of Ω_e is

$$-\frac{1}{a\sin\theta} < \Omega_e < \frac{1}{a\sin\theta}. \quad (32)$$

For $\Omega_e = 0$, Eq.(30) reduces to

$$|\vec{\Omega}_p| = \frac{M}{a^2} \tan\theta \sec^2\theta \quad (33)$$

which can be seen from Eq.(6) and (7) of Ref.[3]. The above equation shows that Ω_p varies from $0 \leq \Omega_p < \infty$ for $0 \leq \theta < 90^\circ$ at $r = 0$. Thus, it is finite inside the ring singularity ($x^2 + y^2 < a^2$, $z = 0$) but diverges only on it (which is at $x^2 + y^2 = a^2$, $z = 0$).

It is useful to mention here that one can smoothly, in principle, go over to the region with ‘negative r ’ (i.e., $r < 0$) in Kerr spacetime, which is tantamount to passing through the ring singularity but we stop at $r = 0$ and avoid probing negative values of r . The reason behind stopping at $r = 0$ is that it is fairly widely accepted that quantum gravity will resolve the singularity resulting in a compact overspinning object with boundary at a positive value of r , which is referred to as ‘superspinar’ [11]. Thus the region with negative values of r will be excised and pathological features such as closed timelike curves which occur in $r < 0$ region will not arise. Thus we restrict our probe of the Kerr spacetime to $r \geq 0$.

B. Behavior of gyro frequency in the equatorial plane, $\theta = \pi/2$

The gyro precession frequency along the equatorial plane is given as,

$$\vec{\Omega}_p|_{\theta=\pi/2} = \frac{aM + \Omega_e(r^3 - 3Mr^2 - 2Ma^2) + aM\Omega_e^2(3r^2 + a^2)}{r^2[(r - 2M) + 4\Omega_e Ma - \Omega_e^2[r(r^2 + a^2) + 2Ma^2]]} \quad (34)$$

with the range Ω_e determined from Eq.(26).

In the equatorial plane, at the ergosurface ($r = 2M$) the precession frequency becomes

$$\vec{\Omega}_p|_{\theta=\pi/2, r=2M} = \frac{a - 2\Omega_e(a^2 + 2M^2) + a\Omega_e^2(a^2 + 12M^2)}{16\Omega_e M^2[a - \Omega_e(a^2 + 2M^2)]} \quad (35)$$

where, we obtain the range of Ω_e as (see FIG.1 also)

$$0 < \Omega_e < \frac{a}{a^2 + 2M^2}. \quad (36)$$

That is, if the mass and/or the angular momentum of the spacetime increases, Ω_e decreases.

Specifically, for extremal BHs ($a_* = 1$), the precession frequencies at the outer ergoregion and at the outer event horizon can be obtained as

$$\vec{\Omega}_p|_{\theta=\pi/2, r=2M, a_*=1} = \frac{1 - 6\Omega_e M + 13\Omega_e^2 M^2}{16\Omega_e M^2[1 - 3\Omega_e M]} ; \quad \vec{\Omega}_p|_{\theta=\pi/2, r=M, a_*=1} = -\frac{1}{M} \quad (37)$$

respectively.

C. Non-zero precession frequency of the test gyro in the Schwarzschild spacetime

Now, if we set $a = 0$, the Kerr spacetime reduces to the Schwarzschild spacetime, which is *non-rotating*. Substituting $a = 0$ in Eq.(19), we obtain

$$\vec{\Omega}_p|_{a=0} = \Omega_e \frac{(r - 3M) \sin \theta \hat{\theta} - (r^2 - 2Mr)^{\frac{1}{2}} \cos \theta \hat{r}}{r - 2M - r^3 \Omega_e^2 \sin^2 \theta} \quad (38)$$

where Ω_e can take any value (provided u should be timelike) and always be timelike. Since the Schwarzschild spacetime is spherically symmetric, we can write Eq.(38) for $\theta = \pi/2$ as

$$\Omega_p|_{a=0} = \Omega_e \frac{r - 3M}{r - 2M - r^3 \Omega_e^2}. \quad (39)$$

This implies that a gyro which is moving in spherically symmetric spacetime, will in fact precess. If the gyro moves along a circular geodesic Ω_e should be the Kepler frequency, i.e., $\Omega_e = (M/r^3)^{1/2}$.

Therefore, Eq.(39) reduces to

$$\Omega_p|_{a=0, \Omega_e=(\frac{M}{r^3})^{\frac{1}{2}}} = \Omega_e = \left(\frac{M}{r^3}\right)^{\frac{1}{2}}. \quad (40)$$

The expression above which gives the precession frequency is expressed in the Copernican frame and is the rate which is computed with respect to the proper time τ . The proper time τ measured in

the Copernican frame is related to the coordinate time t via $d\tau = \sqrt{1 - \frac{3M}{r}} dt$. Thus the precession frequency Ω' in the coordinate basis is given by

$$\Omega' = \left(\frac{M}{r^3}\right)^{\frac{1}{2}} \sqrt{1 - \frac{3M}{r}}. \quad (41)$$

Now, we ask what the frequency associated with the change in the angle of the spin vector over, say, one complete revolution around the central object is. As mentioned above $\Omega_e = \sqrt{M/r^3}$. This becomes one purely of kinematics and using the formalism outlined in [12], one can then write down the frequency of precession, which is actually just the geodetic precession frequency (Ω_{geodetic}). This frequency turns out simply to be the difference between the Kepler frequency and rotation frequency and is given by,

$$\Omega_{\text{geodetic}} = \left(\frac{M}{r^3}\right)^{\frac{1}{2}} \left(1 - \sqrt{1 - \frac{3M}{r}}\right). \quad (42)$$

This agrees with the results quoted in the literature [13].

V. DISTINGUISHING KERR NAKED SINGULARITIES FROM KERR BLACK HOLES USING THE PRECESSION OF A TEST GYRO

In this section, we point out the characteristic differences in the behavior of the spin precession frequency (Ω_p) of test gyroscopes for BHs and NSs. We show that the value of Ω_p diverges for gyroscopes with $r \sim r_+$ in the case of a BH, for all values of q except $q = 0.5$. Whereas, for a NS, Ω_p always remains finite upto $r = 0$. We obtain distinguishing characteristic features in the radial profile of Ω_p for both BH and NS cases, which we will discuss as we proceed. Moreover, we also obtain features in the radial profile of Ω_p that could help distinguish near-extremal NS from higher spin NSs (for eg, near extremal NSs have more than one local maxima and/or local minima and/or plateaus between $0.5M \lesssim r \lesssim M$). We explore the details of such features and argue that they provide us with a possible distinguishing criterion to separate out near-extremal NS ($1 < a_* < 1.1$) from those with higher spins ($a_* \geq 1.1$) (Sec.VI).

Now, substituting the value of Ω_e for different q (see Eq.27) in Eq.(19) and Eq.(20), we can obtain the final expression (Eq.(29)) of $\Omega_p = |\vec{\Omega}_p|$ and plot the gyro precession frequency. For BHs, we can see from all the Panels (a)-(i) of FIG.2 that the precession frequency diverges close to the horizon in all directions for all values of a_* and for all values of q except $q = 0.5$. For $q < 0.5$ (Panels (a) and (b)), the nature of the plots are almost same but for $q > 0.5$, a ‘kink’ appears at some intermediate angles. For very low values of a_* , the ‘kink’ starts to appear close to the equatorial plane and if the value of

a_* is increased the kink starts to appear at a lower angular value. As an example, for $a_* = 0.2$, the kink starts to appear at $\theta = 65^\circ$ (Panel(e)) and it is very prominent at $\theta = 80^\circ$ (Panel(f)) whereas for $a_* = 0.9$, kink starts to appear at $\theta = 40^\circ$ (Panel(h)) and it is more prominent than the previous case at $\theta = 65^\circ$ (Panel(i)). Thus, we can state that the spin precession frequency is finite both inside and outside of the ergoregion and there is no discontinuity at all but it diverges near the horizon.

Remarkably, for $q = 0.5$, the precession frequency remains finite (see Panel(c) and (d) of FIG.2) for gyros orbiting close to the horizon, with the velocity of the gyro proportional to $\partial_t + \Omega_e \partial_\phi$, where Ω_e is obtained from Eq.(28). For all other choices of q in the allowed range, the precession frequency shows a divergence for gyros with $r \sim r_+$.

We have plotted the spin precession frequencies in Panels (a)-(g) of FIG.3 for the NS case ($a_* = 2$). As can be seen from these plots, the spin precession frequencies do not diverge like the BH case but remain finite and regular even as one approaches $r = 0$ for all angles $0 < \theta < 90^\circ$, irrespective of the presence of the ergoregion, as opposed to [3], where it was shown that the spin precession frequency diverges on the ergosurface for NSs. At $\theta = 90^\circ$, the precession frequency diverges because of the presence of the ring singularity. This is also in stark contrast to the BH case in the present paper, for which a divergence is exhibited by the precession frequency close to the event horizon, as discussed earlier. One also finds that a local minima and a local maxima appear for $q \geq 0.5$ in some intermediate angles. As an example, for $q = 0.5$, local minima appears very close to the pole ($> 0^\circ$) and disappears at $\sim 60^\circ$ whereas for $q = 0.8$ local maxima-minima starts to appear at $\sim 55^\circ$ and disappears $\sim 86^\circ$. Thus, for higher q value local maxima-minima lasts for shorter angular range. The above mentioned characteristics is not only applicable for $a_* = 2$ but also applicable for all the NS cases of $a_* > 1.1$.

We now detail our experiment to distinguish a NS from a BH. We study the precession of spins of gyros attached to observers with a non-zero azimuthal component ($\Omega_e(r, \theta)$) to their four-velocities, that is $u = (1, 0, 0, \Omega_e)$. These are observers moving along circles at constant r and θ . As discussed earlier, there are no restrictions on Ω_e outside the ergoregion. However, not all values of Ω_e are allowed inside the ergoregion since we want the four-velocities K_e to be time-like. For every curve with fixed (r, θ) inside the ergoregion, we can find the range of allowed $\Omega_e(r, \theta)$ by finding $\Omega_-(r, \theta)$ and $\Omega_+(r, \theta)$. One characteristic feature of the ergoregion is that as one allows Ω_e to approach the bounding values, $\Omega_e \rightarrow \Omega_\pm$, the precession frequency Ω_p exhibits a sharp rise. Now, we consider a set of observers (say, at different r), equipped with gyroscopes, moving on constant r, θ curves around an unknown rotating compact astrophysical object. There are two possible observations one can make when one measures the precession frequency of the spins of gyroscopes attached to such observers, with progressively decreasing

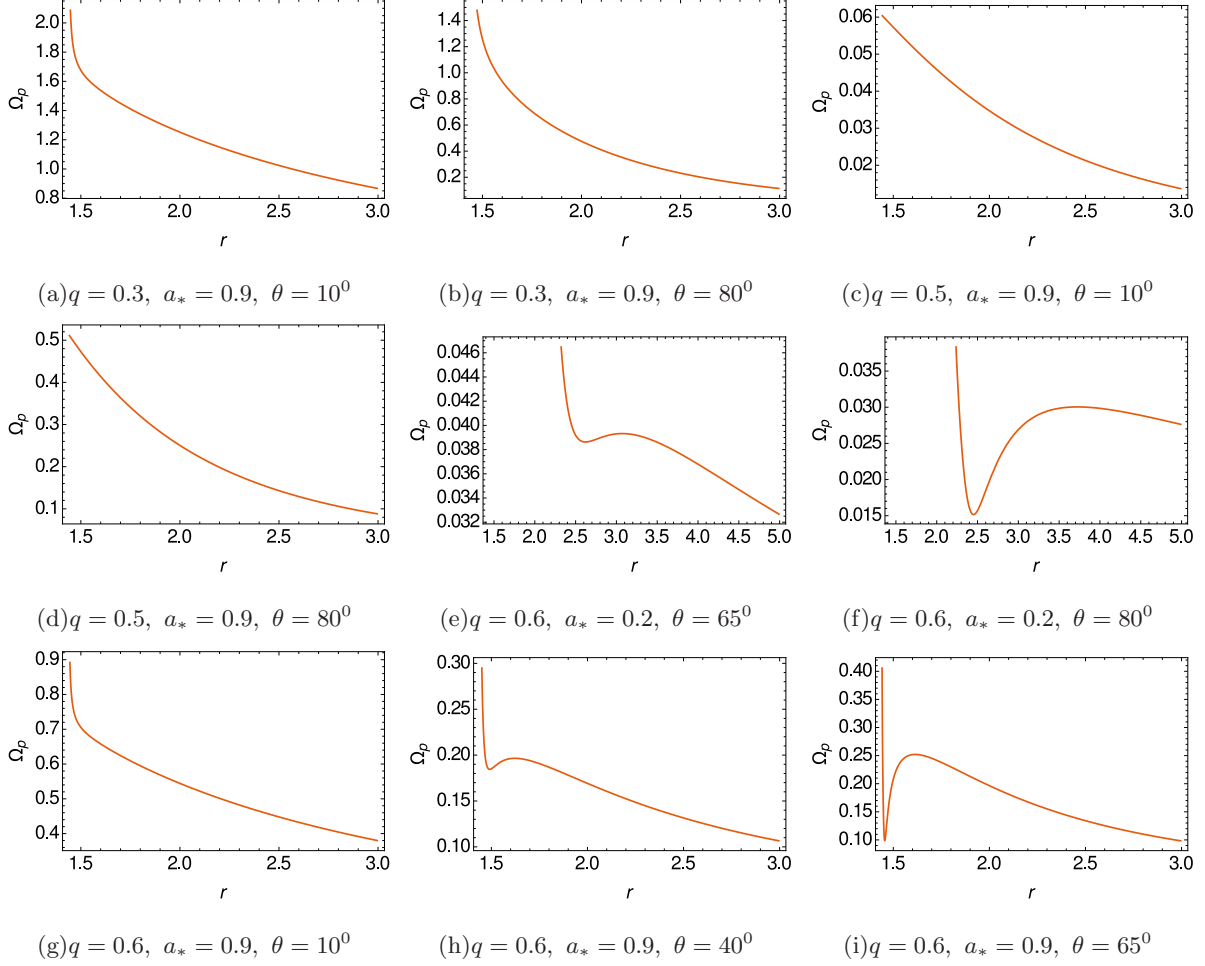


FIG. 2. Variation of Ω_p (in the unit of M^{-1}) versus r (in the unit of M) in the case of BHs with different Kerr parameters a_* . Gyros approach the BHs from different direction θ with different angular velocity which is parametrized by q . It is seen from the plots that the gyro precession frequency Ω_p becomes arbitrarily high in the limit of approach to the event horizon, thus diverging on the horizon in case of a BH for $q \leq 0.5$ but Ω_p becomes finite only for $q = 0.5$.

r : (i) $\Omega_p(r)$ continually increases (we may also see features like those in Panels (f) and (i) of FIG.2) and after crossing a certain distance it diverges eventually; or (ii) it increases and after crossing a certain distance it decreases continuously and remains finite throughout (we may also see features like those in Panels (c) and (f) of FIG.3). Then we can conclude that in a Kerr spacetime, Case (i) signals that the spacetimes is that of a BH whereas, Case (ii) implies that we have a NS instead.

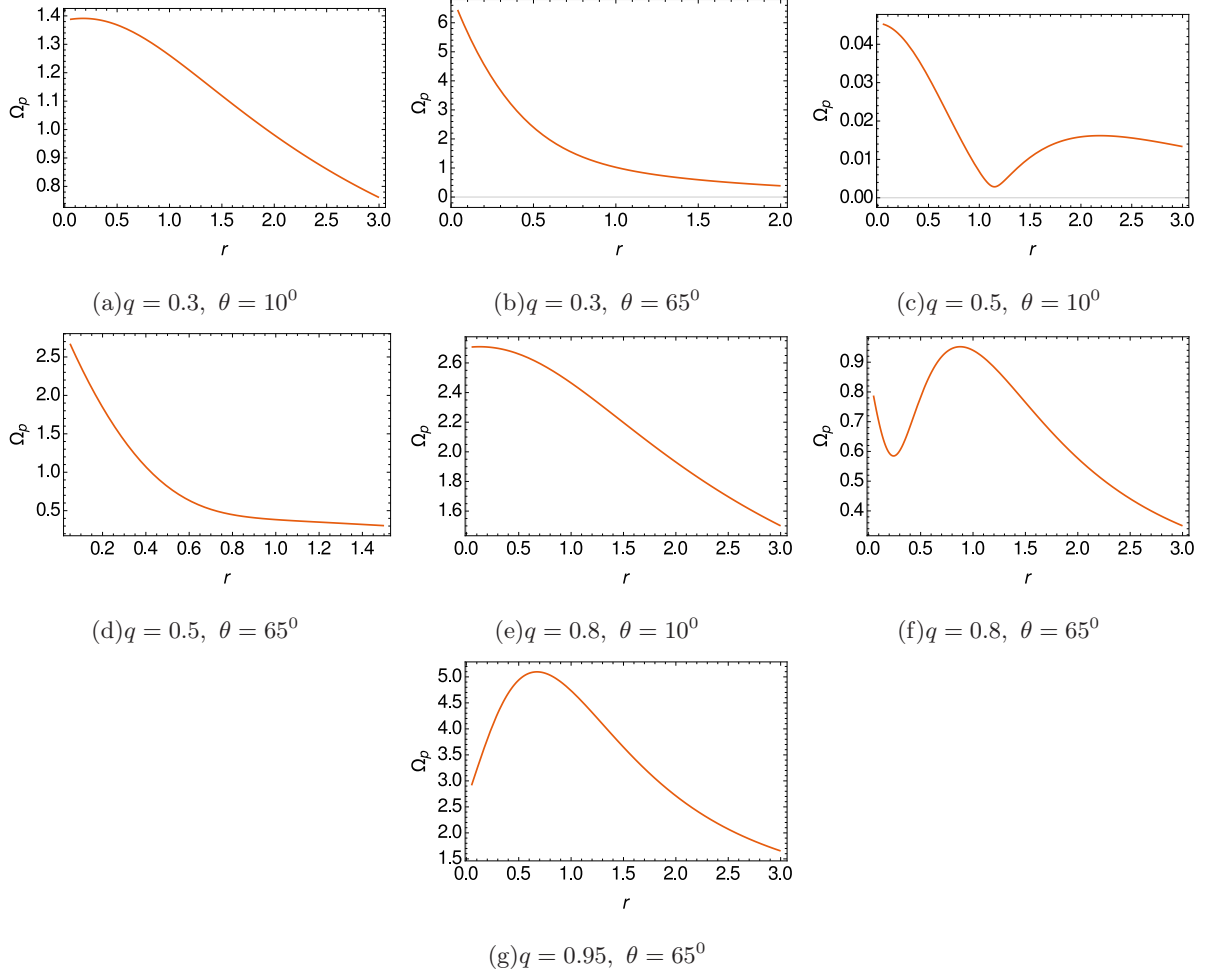


FIG. 3. Variation of Ω_p (in the unit of M^{-1}) versus r (in the unit of M) in the case of NS with $a_* = 2$. Gyros approach the NSs from different direction θ with different angular velocity which is parametrized by q . It is seen from the plots that the gyro precession frequency Ω_p is finite in all the way as the gyro approaches $r = 0$ from any angular direction : $0 < \theta < \pi/2$. Moreover, Ω_p remains finite even at $r = 0$ for all the values of q : $0 < q < 1$.

VI. DISTINGUISHING A NEAR-EXTREMAL KERR NAKED SINGULARITY ($1 < a_* < 1.1$) FROM A KERR NAKED SINGULARITY WITH HIGHER ANGULAR MOMENTUM ($a_* \geq 1.1$)

A. Behavior of gyro frequency for q values close to 0.5 ($q \sim 0.5$)

A near-extremal NS ($a_* < 1.1$) exhibits characteristically different features as compared to NSs with higher spins, that is we do not observe trends like those in FIG.3 for near-extremal NSs. Moreover, observed features are extremely dependent on q values. Two minima occur for intermediate values of θ when spin parameter is close to one and q close to 0.5. We can see from FIG.4 that two minima occur

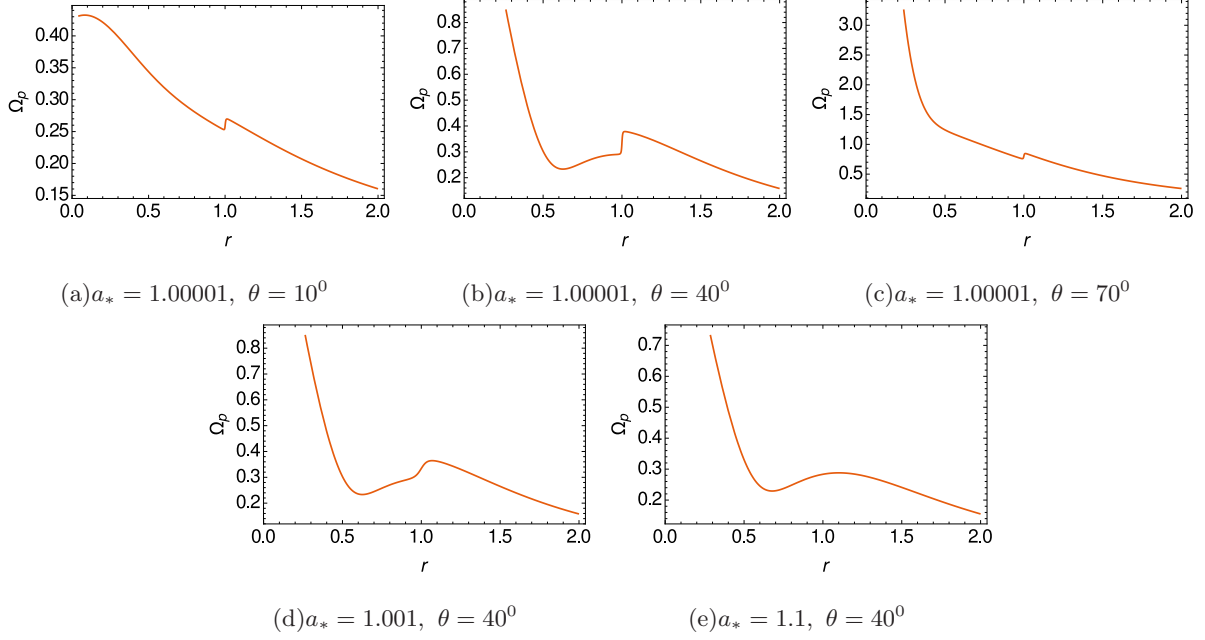


FIG. 4. Variation of Ω_p (in the unit of M^{-1}) versus r (in the unit of M) in the case of near-extremal NSs. Gyros approach the NSs from different direction θ with a fixed angular velocity which is parametrized by $q = 0.47$. It is seen from the plots that the gyro precession frequency Ω_p is finite in all the way as the gyro approaches $r = 0$ from any angular direction : $0 < \theta < \pi/2$. Moreover, Ω_p remains finite even at $r = 0$ for all the values of q : $0 < q < 1$. It is also seen from the plots that an interesting interplay between the local maxima and/or local minima go on in all the curves, which lasts only for $1 < a_* < 1.1$.

at the angle 40° (Panel(b) and Panel(d)) and its nearby angles for $q = 0.47$. One minima disappears around $\sim 70^\circ$ and another one still remains (Panel(c)). These all ‘peculiarities’ go away when we increase the spin parameter further, i.e., $a_* \geq 1.1$.

Similarly, we can see from Panels (a)-(c) of FIG.5 that the two minima occur at some intermediate angles for $q = 0.51$ and start to disappear at $\theta = 60^\circ$ (Panel (d)). The one minima also disappears if a_* possesses a value further away from 1 ($a_* \geq 1.1$), which can be seen from Panels(f)-(g).

When spin is close to one, there is a also sharp rise in frequency very close to $r = M$, for intermediate values of θ when q is slightly larger than 0.5 and sharp decline when q is slightly below 0.5. Such sharp increase/decrease is absent when a_* is larger than 1.01. So, there are two peculiar features associated with the near-extremal geometries in this case: (i) presence of two minima, and (ii) sharp rise or fall of frequencies close to $r = M$. The second feature is due to ‘phantom effects’ of the horizon, something we will try to address in a later section on near extremal NS.

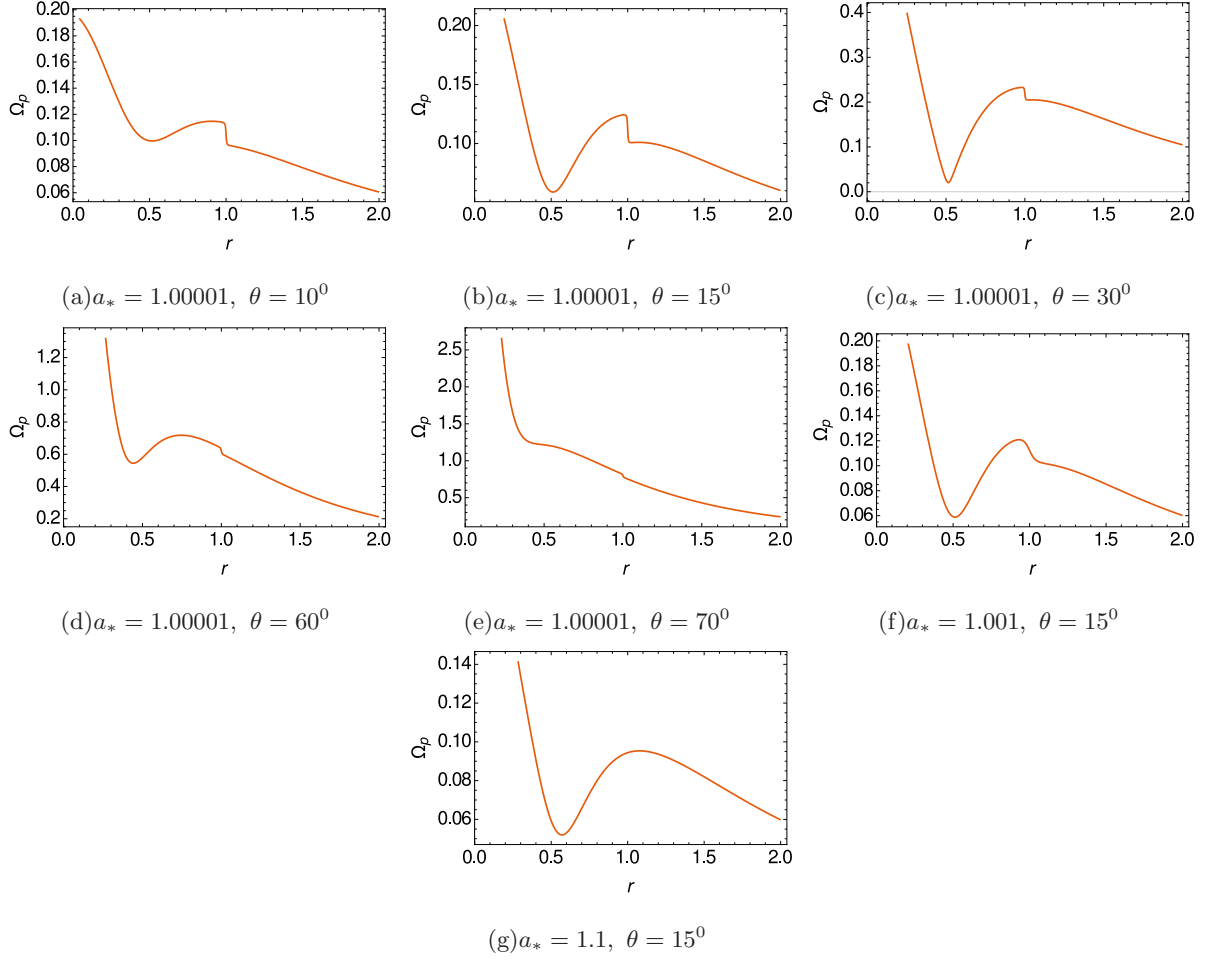


FIG. 5. Same as FIG.4 but has been plotted for $q = 0.51$.

B. Behavior of gyro frequency for $q < 0.5$

For $q < 0.5$, a small kink appears in the radial profile of the gyro precession frequency, which can be seen from Panels(a)-(c) of FIG.6. The kink disappears for higher values of spin parameter. In this case, we can also see that the kink is basically a sharp rise in frequency close to $r = M$. Similar trends in the radial profiles of these frequencies can be observed for all values of $q < 0.5$ but not for values close to 0.5 like in FIG.4.

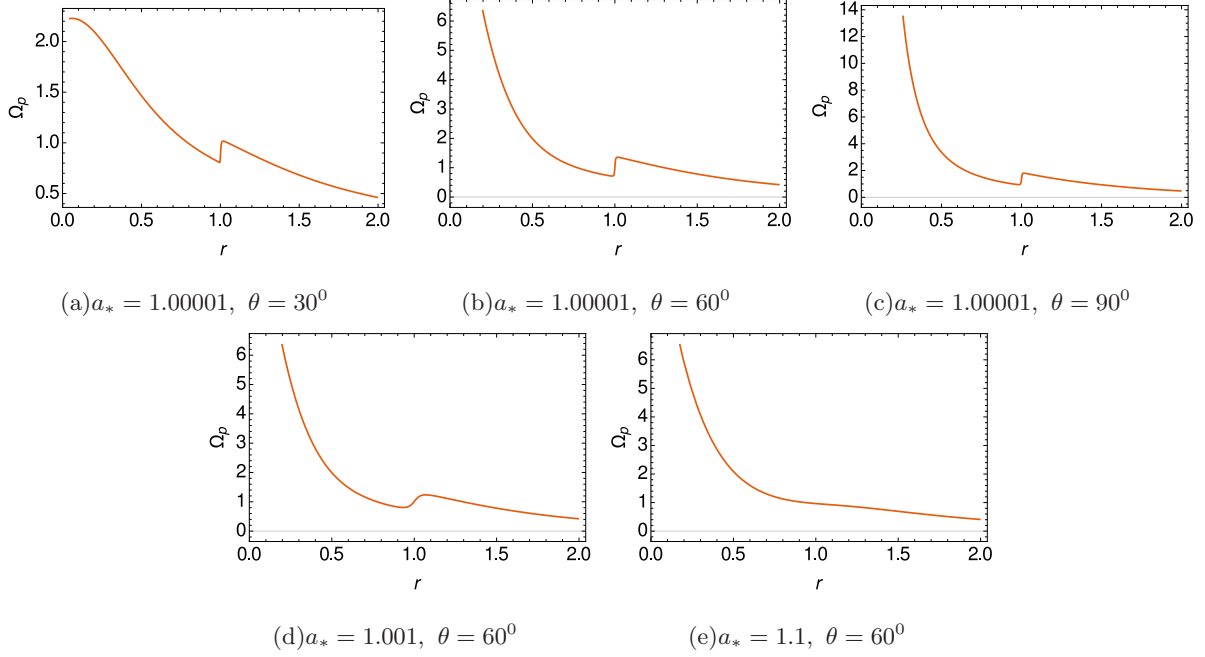


FIG. 6. Same as FIG. 4 but has been plotted for $q = 0.3$.

C. Behavior of gyro frequency for $q > 0.5$

1. $q = 0.7$

For $q > 0.5$, we can see from Panel (a) of FIG. 7 that a kink starts to appear at $\theta = 20^\circ$ and it becomes a sharp rise (Panels (b)-(c)) at $r = M$, on increasing the value of the angle. Three peaks appear at $\theta = 80^\circ$ (Panel (d) and Panel (h)) with a plateau between two peaks. This special feature disappears at $\theta = 88^\circ$. It also disappears for higher values of the spin parameter a_* which can be seen from Panels (g) and (i). The spin precession frequency value at the third peak (which is very close to $r = 0$), is much higher than at the other two. All these special features go away for $a_* > 1.1$ (Panel (i)) for intermediate angles.

2. $q = 0.9$

For very high values of q , say $q = 0.9$, we can see from all the Panels (a)-(e) of FIG. 8 that the ‘third peak’ (which appeared for $q = 0.7$) near $r = 0$ disappears but the ‘sharp rise’ at $r = M$ still remains there for some intermediate range of angles (Panel(b)-(d)). At $\theta = 80^\circ$ (Panel (c)), there exists ‘two peaks’ with the plateau. Only one peak remains for $a \geq 1.1$ as usual, which is generally seen in the

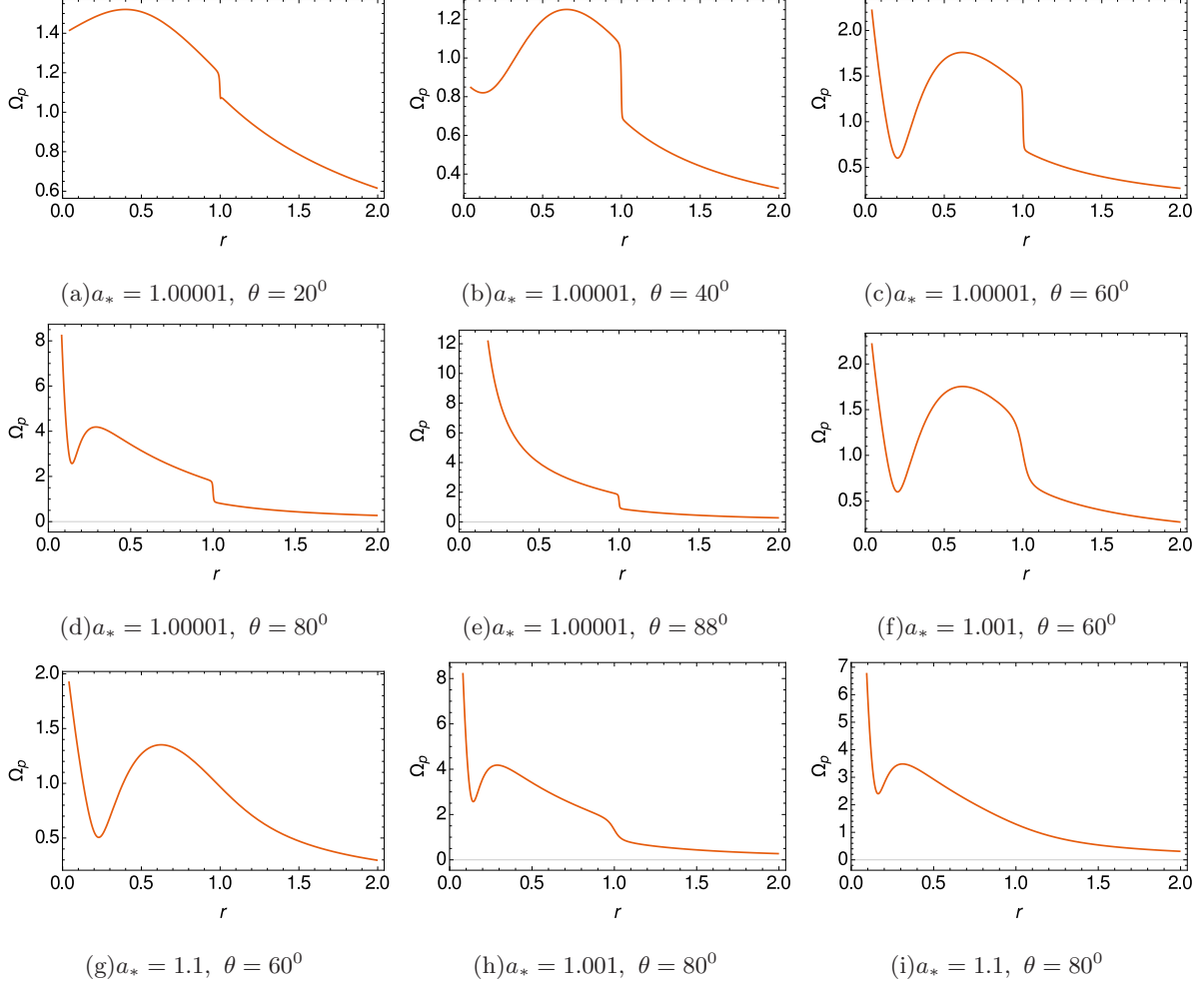


FIG. 7. Same as FIG.4 but has been plotted for $q = 0.7$.

cases of the NSs which possesses higher angular momentum (see FIG.3).

D. Behavior of gyro frequency for near-extremal Superspinars

We replace a everywhere in Eq.(19) with $M(1 + \epsilon)$ and drop terms containing order ϵ^2 or higher. We introduce the dimensionless variables $y = r/M$ and $\omega_e = M\Omega_e$ and write the components of the

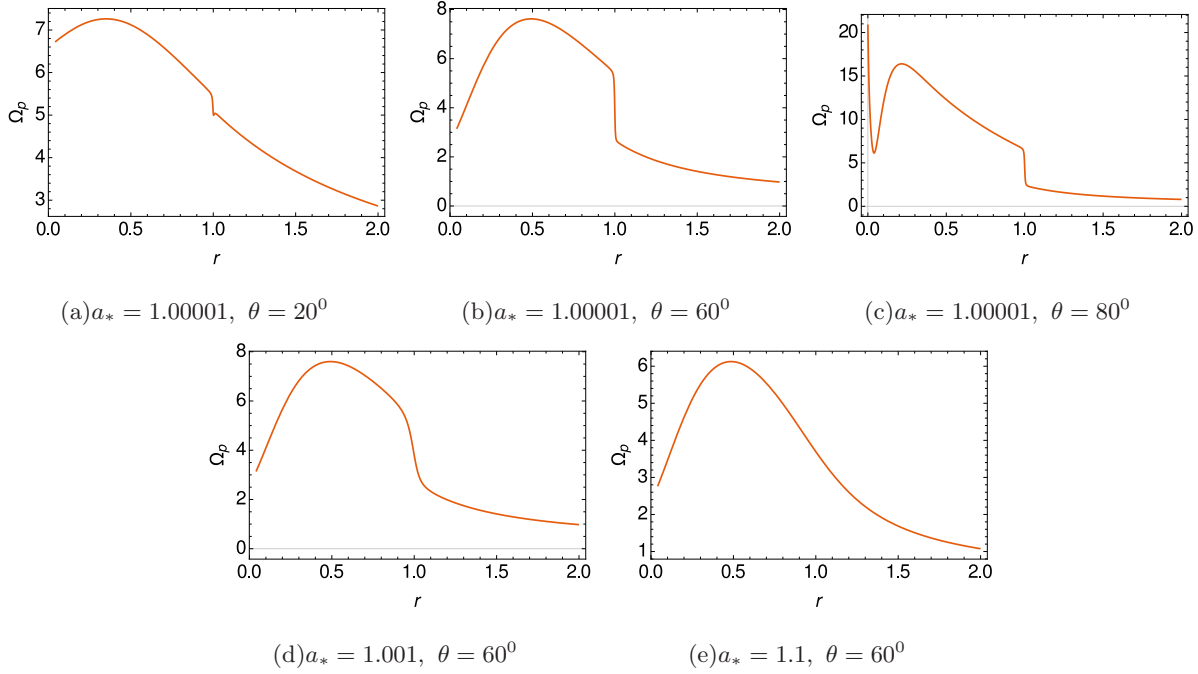


FIG. 8. Same as FIG.4 but has been plotted for $q = 0.9$.

spin precession frequency as

$$\Omega_p \hat{r} = \frac{1}{M} \frac{(y-1) \cos \theta}{(y^2 + \cos^2 \theta)^{3/2}} \frac{A_1}{D_1} \left[1 + \epsilon \left(\frac{A_2}{A_1} + \frac{1}{(y-1)^2} - \frac{3 \cos^2 \theta}{y^2 + \cos^2 \theta} - \frac{D_2}{D_1} \right) \right] \hat{r}, \text{ when } (y-1)^2 \gg \epsilon$$

$$= \frac{\epsilon}{M} \frac{(y-1) \cos \theta}{(y^2 + \cos^2 \theta)^{3/2}} \frac{A_1}{D_1} \hat{r}, \quad \text{otherwise}$$

and,

$$\Omega_p \hat{\theta} = \frac{1}{M} \frac{\sin \theta}{(y^2 + \cos^2 \theta)^{3/2}} \frac{B_1}{D_1} \left[1 + \epsilon \left(\frac{B_2}{B_1} - \frac{3 \cos^2 \theta}{y^2 + \cos^2 \theta} - \frac{D_2}{D_1} \right) \right] \hat{\theta} \quad (43)$$

where,

$$A_1 = -\omega_e y^4 - 2\omega_e \cos^2 \theta y^2 + 2(1 - \omega_e \sin^2 \theta)^2 y - \frac{\omega_e}{8}(3 + 4 \cos 2\theta + \cos 4\theta),$$

$$A_2 = -4\omega_e \cos^2 \theta y^2 + 2(1 - \omega_e \sin^2 \theta)(1 - 3\omega_e \sin^2 \theta)y - \frac{\omega_e}{2}(3 + 4 \cos 2\theta + \cos 4\theta),$$

$$B_1 = \omega_e y^5 - 3\omega_e(1 - \omega_e \sin^2 \theta)y^4 + 2\omega_e \cos^2 \theta y^3 + (1 - \omega_e \sin^2 \theta)(1 - \omega_e(1 + \cos^2 \theta))y^2$$

$$+ \omega_e \cos^4 \theta y - \cos^2 \theta(1 - \omega_e),$$

$$B_2 = 3\omega_e^2 \sin^2 \theta y^4 + 4\omega_e \cos^2 \theta y^3 + (1 - 4\omega_e + 3\omega_e^2 - 3\omega_e^2 \cos^4 \theta)y^2 + 4\omega_e \cos^4 \theta y$$

$$- \cos^2 \theta(3 - 4\omega_e(1 + \sin^2 \theta) + 5\omega_e^2 \sin^2 \theta),$$

$$D_1 = -\omega_e^2 \sin^2 \theta y^4 + [1 - \omega_e^2 \sin^2 \theta(1 + \cos^2 \theta)]y^2 - 2[1 - \omega_e \sin^2 \theta]^2 y + \cos^2 \theta[1 - \omega_e^2 \sin^2 \theta],$$

$$D_2 = -2\omega_e^2 \sin^2 \theta(1 + \cos^2 \theta)y^2 + 4\omega_e \sin^2 \theta(1 - \omega_e \sin^2 \theta)y + 2 \cos^2 \theta(1 - 2\omega_e^2 \sin^2 \theta). \quad (44)$$

The above expressions simplify greatly for the equatorial plane $\theta = \pi/2$ as

$$\begin{aligned}
A_1 &= -\omega_e y^4 + 2(1 - \omega_e)^2 y \\
A_2 &= 2(1 - \omega_e)(1 - 3\omega_e)y \\
B_1 &= \omega_e y^5 - 3\omega_e(1 - \omega_e)y^4 + (1 - \omega_e)^2 y^2 \\
B_2 &= 3\omega_e^2 y^4 + (1 - 4\omega_e + 3\omega_e^2)y^2 \\
D_1 &= -\omega_e^2 y^4 + (1 - \omega_e^2)y^2 - 2(1 - \omega_e)^2 y \\
D_2 &= -2\omega_e^2 y^2 + 4\omega_e(1 - \omega_e)y
\end{aligned} \tag{45}$$

and a simple but qualitative analytic treatment of the problem is admitted. We can then discuss the number of poles and peaks of the spin precession frequency of near extremal superspinars inside the ergoregion, confining ourselves to the equatorial plane.

From the above expressions it is clear that the radial part of this frequency vanishes everywhere in the equatorial plane of the ergoregion except at the ring singularity, for all allowed frequencies Ω_e . The angular part of this gyro frequency in the equatorial plane is

$$\vec{\Omega}_p = \frac{1}{M} \frac{1}{y^3} \frac{B_1}{D_1} \left[1 + \epsilon \left(\frac{B_2}{B_1} - \frac{D_2}{D_1} \right) \right] \hat{\theta} \tag{46}$$

$$\begin{aligned}
M\vec{\Omega}_p &= \frac{\omega_e y^3 - 3\omega_e(1 - \omega_e)y^2 + (1 - \omega_e)^2}{-\omega_e^2 y^5 + (1 - \omega_e^2)y^3 - 2(1 - \omega_e)^2 y^2} \hat{\theta} + \epsilon \frac{\omega_e y^3 - 3\omega_e(1 - \omega_e)y^2 + (1 - \omega_e)^2}{-\omega_e^2 y^5 + (1 - \omega_e^2)y^3 - 2(1 - \omega_e)^2 y^2} \cdot \\
&\quad \left(\frac{3\omega_e^2 y^2 + (1 - 4\omega_e + 3\omega_e^2)}{\omega_e y^3 - 3\omega_e(1 - \omega_e)y^2 + (1 - \omega_e)^2} - \frac{-2\omega_e^2 y + 4\omega_e(1 - \omega_e)}{-\omega_e^2 y^3 + (1 - \omega_e^2)y - 2(1 - \omega_e)^2} \right) \hat{\theta}
\end{aligned} \tag{47}$$

Preliminarily, we find that the derivative of the above expression for the gyro frequency vanishes at a maximum of six radial values, that is, for near extremal superspinars, depending on the two parameters Ω_e and a , we can have six local extrema. To further rule a few of these six out, more numerical work needs to be done and this is currently under progress.

E. Behavior of gyro frequency in near-extremal overspinning Kerr geometry and ultra-high energy collisions

Many interesting physical processes occur in near-extremal Kerr geometry at $r = M$. These processes include ultra-high energy particle collisions and collisional Penrose process with extremely large efficiency of energy extraction.

In [14, 15], we considered two particles which follow geodesic motion on the equatorial plane of overspinning Kerr geometry starting from rest at infinity and undergo a collision at $r = M$. One of the

particles that is initially ingoing, turns back at radial coordinate $0 < r < M$ and appears at $r = M$ as an outgoing particle, while the second particle is ingoing. We showed that the center of mass energy of collision between the radially ingoing and outgoing particles shows divergence in the near-extremal limit where Kerr spin parameter transcends the extremal value by an infinitesimal amount, i.e., $a = M(1 + \epsilon)$ with $\epsilon \rightarrow 0^+$. This process overcomes many limitations and finetunings involved in an analogous high-energy collision process between the two ingoing particles which occurs close to the event horizon of the maximally spinning BH [16, 17].

We further showed that the particles which are produced in the ultra-high energy particle collisions in the overspinning Kerr spacetime can escape to infinity with divergent energies [18]. This is a consequence of the collisional Penrose process which allows us to extract rotational energy from the ergoregion of the Kerr spacetime. The efficiency of the collisional Penrose shows divergence in the near-extremal limit for the collisions which occur at $r = M$, making it possible to extract large amount of energy from the overspinning Kerr geometry. This is in the stark contrast with the BH case where efficiency is shown to be always finite with an upper bound of 14 [19]. Thus near-extremal NS spacetime can possibly be the source of the ultra-high energy cosmic rays and neutrinos.

Interestingly, as we showed earlier in this section, gyro precession frequency shows a sharp increase or decline close to $r = M$ in near-extremal overspinning Kerr spacetime as we decrease its radial coordinate along the constant value of θ . This is precisely the location where ultra-high energy collisions and collisional Penrose process with divergent efficiency occurs. Thus a thought experiment to lower gyro which we described in this paper kills two birds with the same bullet. Firstly it allows us to identify the spacetime geometry which is conducive to the high-energy processes as it can tell us whether the geometry is overspinning and near-extremal. Secondly it also helps us to locate region in space which can host high-energy processes as gyro frequency exhibits peculiar trend exactly at this location. This coincidence is quite remarkable.

VII. FRAME-DRAGGING EFFECT IN ACCRETION DISKS IN A KERR GEOMETRY

In order to study the accretion disk around a spinning BH, one needs to study the stable circular orbits in the Kerr space-time. The last or innermost stable circular orbit (ISCO) marks the inner boundary of this disk. The ISCO radius depends on the Kerr parameter a_* , as shown in FIG. 9. This is a key underlying physical feature that can distinguish BHs from NSs, as we will see in this section.

The three fundamental frequencies for the accretion disk, namely the Keplerian frequency Ω_ϕ , vertical epicyclic frequency Ω_θ , and the radial epicyclic frequency Ω_r are derived for the Kerr metric [20, 21]

(in geometrized units) as,

$$\Omega_\phi = \pm \frac{M^{\frac{1}{2}}}{(r^{\frac{3}{2}} \pm aM^{\frac{1}{2}})} \quad (48)$$

$$\Omega_r = \Omega_\phi \left(1 - \frac{6M}{r} \pm \frac{8aM^{\frac{1}{2}}}{r^{\frac{3}{2}}} - \frac{3a^2}{r^2} \right)^{\frac{1}{2}} \quad (49)$$

$$\Omega_\theta = \Omega_\phi \left(1 \mp \frac{4aM^{\frac{1}{2}}}{r^{\frac{3}{2}}} + \frac{3a^2}{r^2} \right)^{\frac{1}{2}} \quad (50)$$

where the upper sign is applicable for direct orbit and the lower one for retrograde orbit. These frequencies are related to the precession of the orbit and orbital plane. Precession of the orbit is measured by the periastron precession frequency (Ω_{per}), and orbital plane precession is measured by the nodal plane precession or Lense-Thirring precession frequency (Ω_{nod}) [22]. These two frequencies are defined as [23]

$$\Omega_{\text{per}} = \Omega_\phi - \Omega_r, \quad (51)$$

$$\Omega_{\text{nod}} = \Omega_\phi - \Omega_\theta. \quad (52)$$

Orbital plane precession arises only due to the rotation of the spacetime. In a non-rotating spacetime, Ω_ϕ is always equal to Ω_θ , and hence the Lense-Thirring precession is entirely absent. However, periastron precession occurs both in rotating and non-rotating spacetimes. We note that the square of the radial epicyclic frequency Ω_r^2 vanishes at the ISCO, and is negative for smaller radii, which shows a radial instability for such orbits. Outside the ISCO, Ω_r^2 is always positive and Ω_θ^2 is always non-zero and positive in a rotating spacetime. The same cannot be said about Ω_{nod} . For example, the LT precession frequency (Eq.(52)) can be zero at $r = r_0$ given by,

$$\Omega_{\text{nod}}(r_0) = 0 \Rightarrow r_0 = \frac{9}{16} a_*^2 M = 0.5625 a_*^2 M. \quad (53)$$

Since r_0 is always less than r_{ISCO} ($6M \geq r_{\text{ISCO}} \geq M$ [24]) and even inside the event horizon for a BH ($0 \leq a_* \leq 1$), the LT precession frequency never becomes zero for a BH spacetime. We now discuss the location of the ISCO in a NS spacetime and argue that its relation with r_0 has implications for distinguishing BH and NS spacetimes.

FIG. 9 shows that the ISCO radius decreases with increasing a_* for prograde orbits for both BHs and NSs up to $a_* = \sqrt{32/27} \approx 1.089$, and then increases [25]. Therefore, the minimum ISCO radius, having the value $r_{\text{ISCO}} = 2M/3$, occurs for $a_* = 1.089$. As seen from FIG. 9, the ISCO lies on or inside the ergosurface for $0.943 \leq a_* \leq 2.838$. For each a_* value, there exists a radius (r_0) at which there is no frame-dragging effect, and hence the LT precession vanishes. This radius is less than the

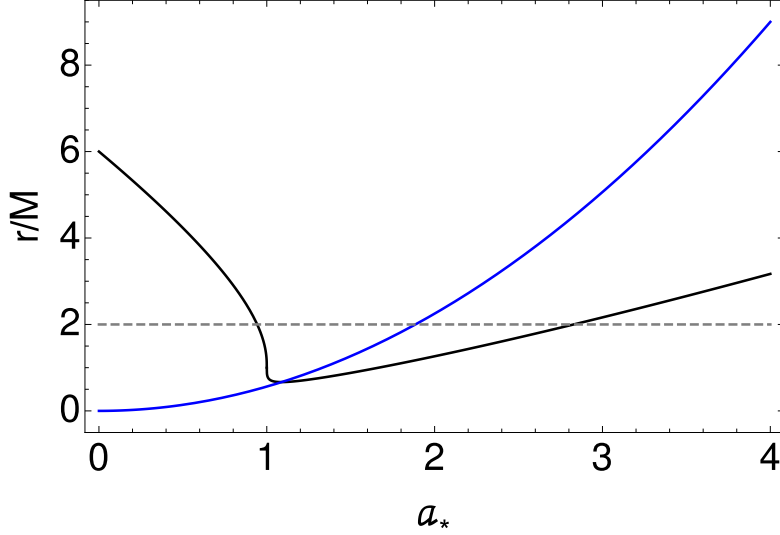


FIG. 9. Three radial quantities (in units of M) for prograde orbits, namely the ISCO radius (black), the ergoradius (dashed gray), and the radius (r_0) at which the precession frequency (Ω_{nod}) vanishes (blue), plotted as functions of the dimensionless Kerr parameter $a_* = a/M$. The ISCO radius lies outside the ergoregion for all a_* except $0.943 \leq a_* \leq 2.838$. r_0 meets the ISCO radius at $a_* = 1.089$. This has the implication that for smaller values of a_* , the LT frequency is always positive and does not vanish for any radius. For larger values, there is a domain of r for which this frequency becomes negative, signifying that the LT effect switches sign. Since this feature is exhibited for $a_* = 1.089 > 1$, the LT frequency in a BH spacetime never vanishes. We point out that NSs with $a_* < 1.089$ also do not display vanishing LT frequency.

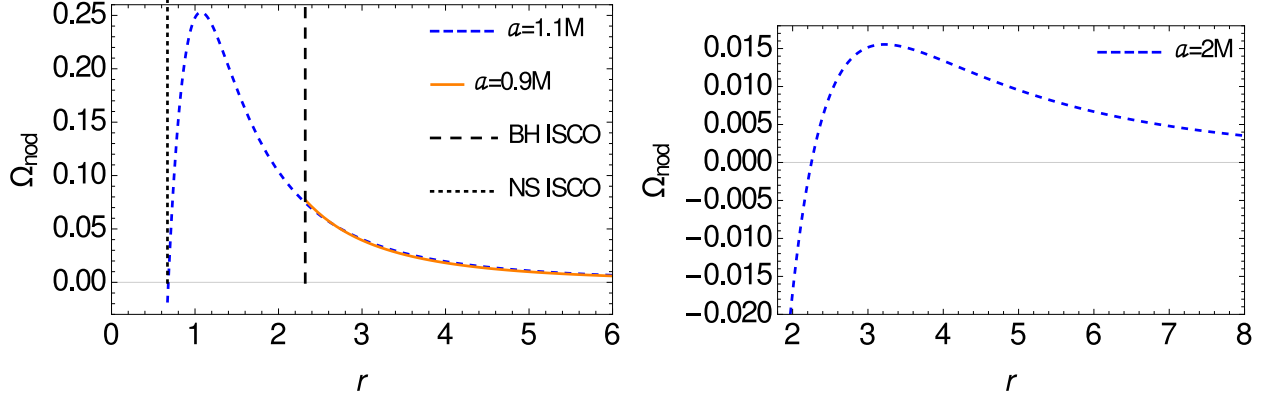
ISCO radius for $a_* < 1.089$ (FIG. 9), but this may not be observationally important, as the accretion disk extends up to r_{ISCO} . FIG. 9 also shows that r_0 equals r_{ISCO} for $a_* = 1.089$ [26], and is greater than r_{ISCO} for $a_* > 1.089$. These make 1.089 a special value of a_* .

In case of BHs, the LT frequency increases with decreasing r up to the inner edge of the accretion disk (see FIG. 10 and Panel (a) of FIG. 11). But for NSs, the LT frequency attains a maximum at $r = r_p$ which occurs always at $r(r = r_p) > r_{\text{ISCO}}$ (see TABLE I), and then decreases as r decreases (FIG. 10 and Panel(b) of 11). As shown in FIGs. 9, 10 and Panel (b) of 11, the LT precession frequency becomes negative for $r_{\text{ISCO}} \leq r < r_0$, in case of $a_* > 1.089$. This means that the direction of LT precession is reversed. The maximum value of Ω_{nod} ($= 1/2M$) occurs for $a_* = 1$ at $r = r_{\text{ISCO}}$. We also note that

$$\left. \frac{d\Omega_{\text{nod}}}{dr} \right|_{r_{\text{ISCO}}} < 0 \text{ for BH,} \quad (54)$$

$$\left. \frac{d\Omega_{\text{nod}}}{dr} \right|_{r_{\text{ISCO}}} > 0 \text{ for NS,} \quad (55)$$

and hence Ω_{nod} decreases (increases) with r at r_{ISCO} for BHs (NSs).



(a) BH ISCO and NS ISCO are located at $2.32 M$ and $0.67 M$ respectively

(b) ISCO is located at $1.26 M$

FIG. 10. Variation of Ω_{nod} (in units of M^{-1}) versus r (in units of M). It is seen from the plots that nodal plane precession frequency Ω_{nod} always increases as one approaches to a BH but in case of a NS, we obtain a peak value of Ω_{nod} for all $a_* > 1$. Ω_{nod} vanishes in a particular orbit of radius r_0 for $a_* \geq 1.089$ and it becomes negative (which means that the LT precession reverses direction) in all the orbits which are in the range $r_0 > r \geq r_{\text{ISCO}}$ for $a_* > 1.089$.

The profiles of other frequencies, i.e., Ω_ϕ , Ω_r , Ω_θ and Ω_{per} , can also show differences between BHs and NSs. FIG. 12 shows that Ω_ϕ behaves similarly for BHs and NSs, but much larger values are possible for the latter, simply because the disk can extend up to much lower radii. FIG. 13 shows that a small additional peak appears in the plot of Ω_r profile for the near extremal value of a_* in the case of a NS. Such a peak appears at small radius values, where an accretion disk cannot exist in case of a BH. As a_* increases, this peak becomes more prominent for $a_* = 1.01$ and it becomes the only peak for $a_* \sim 1.05$. Such an additional peak does not appear for the case of a BH. Similarly, a minimum occurs in the Ω_θ profiles for NSs with $1 < a_* \lesssim 1.1$ near the radius $r = M$ (FIG. 14). Such a minimum does not occur for a BH. Besides, Ω_θ for a_* roughly above 1.01 can attain a much higher value than that for BHs. Finally, the periastron precession frequencies for NSs can attain values much higher than those for BHs (FIG. 15).

Observational aspects

BH X-ray binary (BHXB) sources show a plethora of timing features in X-rays [27]. Most notable among them are high-frequency (HF) quasi-periodic oscillations (QPOs) and three types of low-frequency (LF) QPOs. Sometimes two HF QPOs are seen together. Their frequencies are observed to

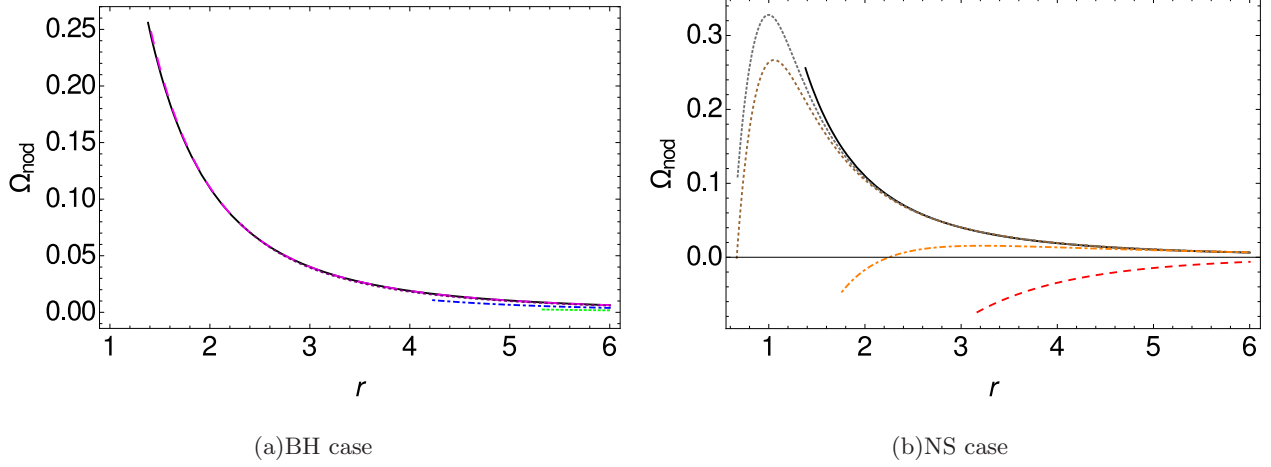


FIG. 11. We show the radial variation of the precession frequency (Ω_{nod}) (in units of M^{-1}) for different a_* BHs in the left panel and NSs on the right panel. For BHs, we plot Ω_{nod} between their respective ISCO radii and $r = 6M$. We have used $a_* = 1$ (black), .9999 (large dashed, magenta), .9 (dotted, purple), .5 (dot-dashed, blue) and .2 (tiny dashed, green). Ω_p decreases with increasing r always for BHs. For NSs, we plot Ω_{nod} between their respective ISCO radii and $r = 6M$. We have included also the extremal BH case to demonstrate the clear change in characteristic features. We have used $a_* = 1$ (black), 1.05 (tiny dashed, gray), 1.089 (dotted, brown), 2 (dot-dashed, orange), 4 (medium dashed, red). For NSs, as we increase r , Ω_{nod} always increases initially at the ISCO radius, reaches a peak value and decreases. Negative Ω_{nod} implies that the sense of precession has changed. These are characteristic features of NSs.

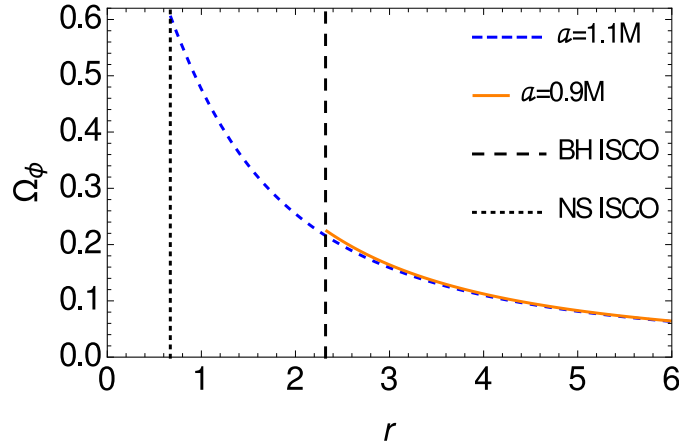


FIG. 12. Variation of Ω_ϕ (in units of M^{-1}) versus r (in units of M). BH ISCO and NS ISCO are located at $2.32 M$ and $0.67 M$ respectively. The plots show that Kepler frequency Ω_ϕ for a NS is much higher than for a BH at their respective ISCOs for $\epsilon = \pm 0.1$, i.e., $a_* = 0.9$ and $a_* = 1.1$. The difference between the values of Kepler frequencies of a NS and a BH decreases with decreasing the value of ϵ .

a_*	r_{ISCO} (in M)	ν_ϕ (in Hz)	ν_θ (in Hz)	ν_{nod} at r_{ISCO} (in Hz)	ν_{nod} (in Hz) at r_p (mentioned in parentheses)
0.1	5.67	234	231	3	
0.2	5.32	255	247	8	
0.3	4.98	279	265	14	
0.4	4.61	309	287	22	
0.5	4.23	346	312	34	
0.6	3.82	395	342	53	
0.7	3.39	458	378	80	
0.8	2.91	552	421	131	
0.9	2.32	718	472	246	
0.98	1.61	1053	462	590	
0.99	1.45	1163	420	743	
0.999	1.18	1395	252	1142	
0.9999	1.07	1510	118	1392	
0.99999	1.03	1556	54	1502	
0.999999	1.016	1572	30	1542	
1.0	1	1591	0	1591	
1.000001	0.98	1615	40	1575	1586 (.998)
1.00001	0.96	1640	84	1556	1584 (.994)
1.0001	0.93	1677	157	1520	1571 (.992)
1.001	0.86	1769	370	1399	1528 (.976)
1.01	0.75	1918	900	1017	1367 (.952)
1.02	0.71	1967	1199	768	1261 (.962)
1.04	0.68	1988	1538	450	1104 (.976)
1.06	0.67	1979	1745	234	1004 (.984)
1.08	0.667	1959	1894	65	886 (1.04)
$\sqrt{32/27}$ ≈ 1.089	2/3	1949	1949	0	847 (1.05)
1.1	0.67	1935	2013	-77	804 (1.07)
2	1.26	932	1588	-655	49 (3.2)
4	3.17	330	566	-236	2 (12.3)
6	5.38	172	288	-116	0.25 (27.7)

TABLE I. An object of mass $M = 10M_\odot (= 15 \text{ km})$ has been considered to calculate ν_ϕ (Kepler frequency), ν_θ (vertical epicyclic frequency) and ν_{nod} (nodal plane precession frequency) using Eq.(48) and Eq.(50). For an example, the conversion factor between ν_ϕ and Ω_ϕ is as follows : ν_ϕ (in kHz) = Ω_ϕ (in km^{-1}) $\cdot \frac{300}{2\pi M}$ and so on. For other values of M , the values of $\nu_\phi, \nu_\theta, \nu_{\text{nod}}$ (column no. 3, 4, 5 & 6) of the table have to be multiplied by $10M_\odot/M$. The values in the parentheses of Column no. 6 show the position of the peak of ν_{nod} .

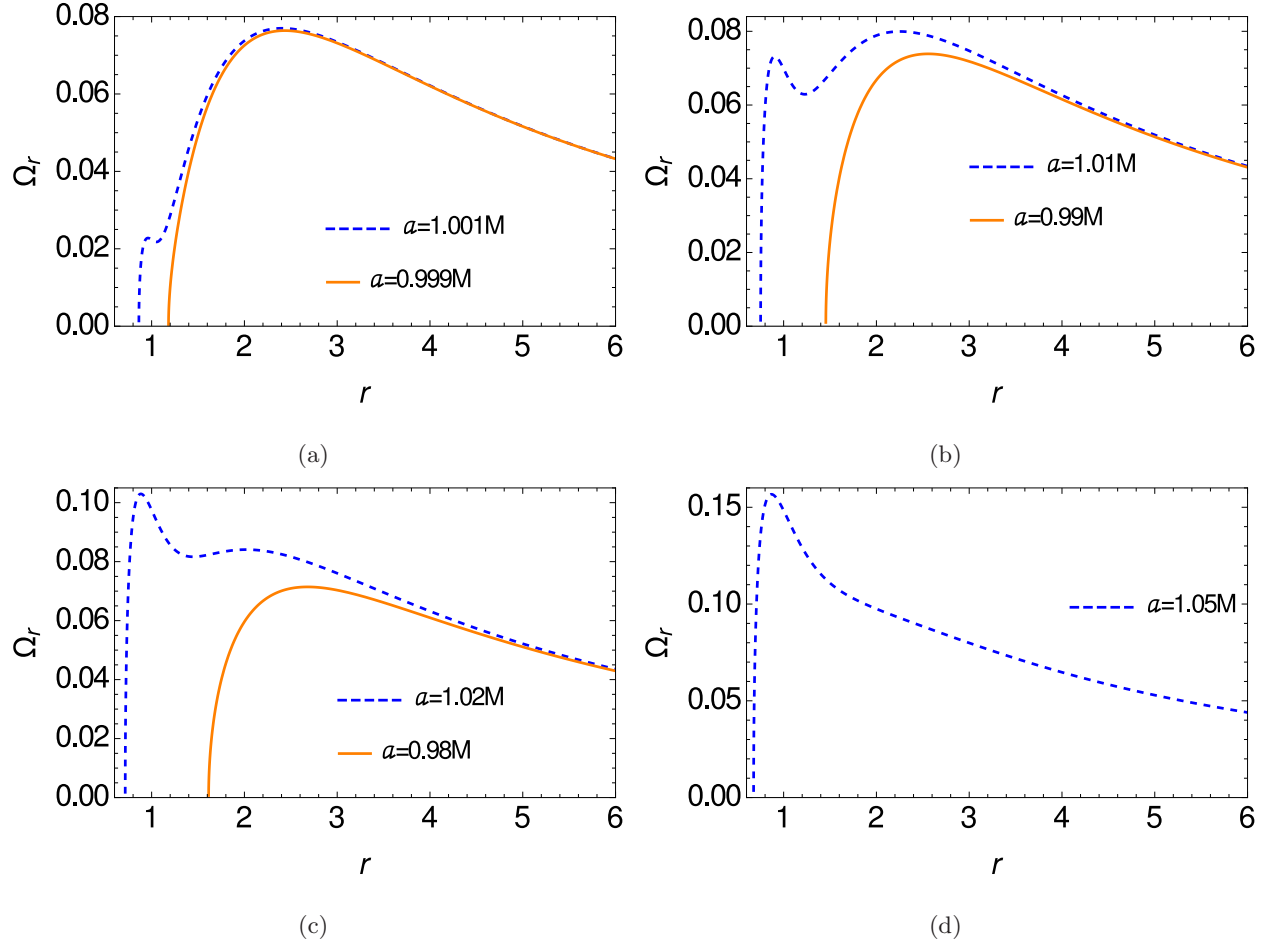


FIG. 13. Variation of Ω_r (in units of M^{-1}) versus r (in units of M). The plots show that Ω_r vanishes at their respective ISCOs of a BH and a NS, which is expected but it can be seen that a small ‘kink’ appears in some of these near-extremal NS cases. This feature is quite clear for $a_* \gtrsim 1.001$ and it disappears for $a_* = 1.05$.

be in the range of several tens to several hundreds of Hz. For example, while XTE 1650–500 has shown HF QPOs in the range of 50 – 270 Hz, 4U 1630–47 has shown such QPOs in 150 – 450 Hz [28]. The three LF QPOs are denoted with types ‘A’, ‘B’ and ‘C’, and their frequencies are typically in the ranges 6.5 – 8 Hz, 0.8 – 6.4 Hz and 0.01 – 30 Hz respectively. While several models exist to explain these QPOs, they are often associated with the relativistic precession (RP) of the accretion disk, and hence with the frequencies Ω_ϕ , Ω_r , Ω_θ , Ω_{per} and Ω_{nod} . The RP model was originally conceived to explain the twin kilo-Hertz (kHz) QPOs and a low-frequency QPO of neutron star low-mass X-ray binaries [29, 30]. Following this idea, frequencies of the C-type LF QPO, the lower frequency HF QPO and the higher frequency HF QPO of BHXBs are identified with Ω_{nod} , Ω_{per} and Ω_ϕ respectively [31]. This can be useful to measure both the mass (M) and a_* of the compact object, as demonstrated by [32]. Table I

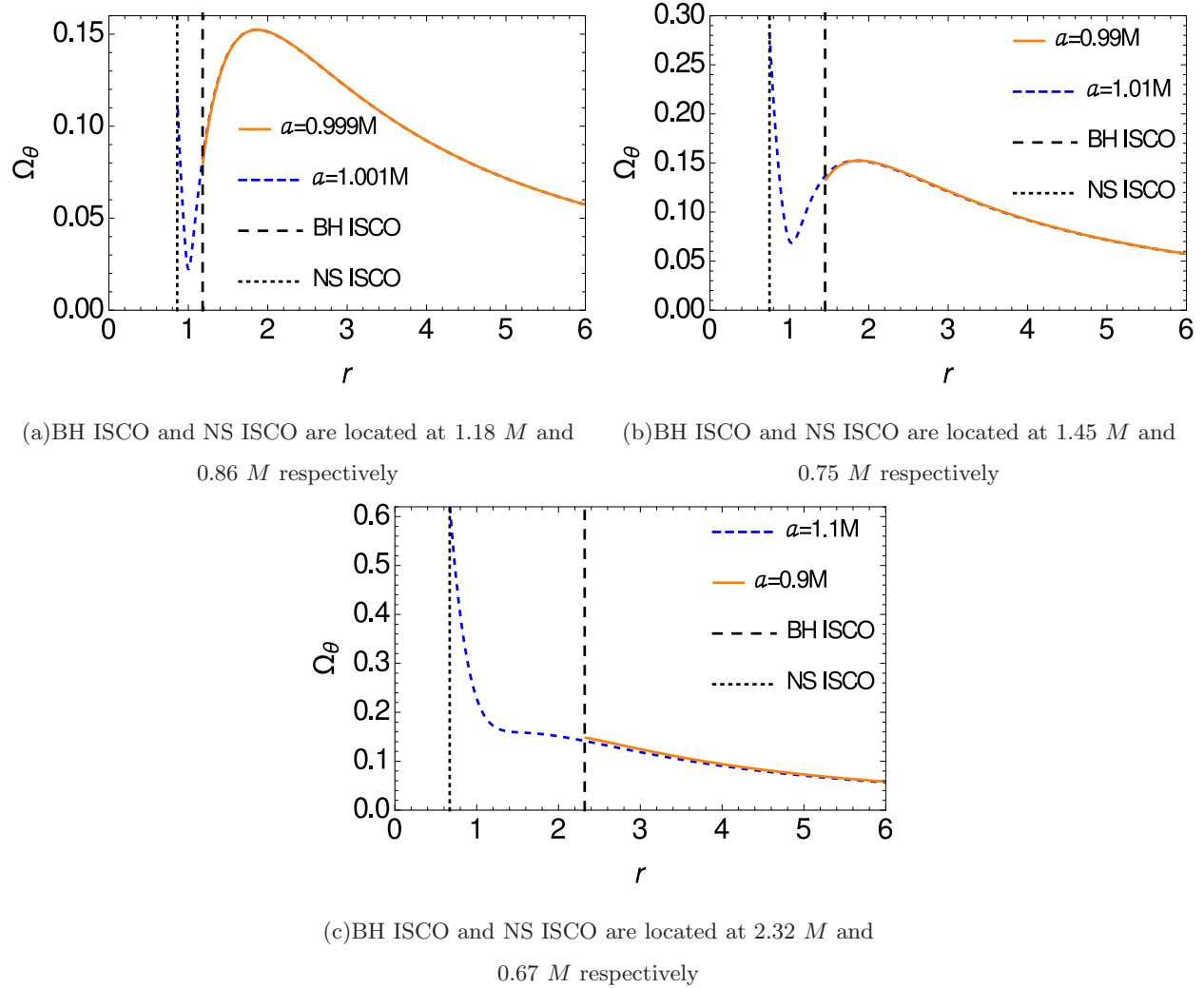


FIG. 14. Variation of Ω_θ (in units of M^{-1}) versus r (in units of M). The plots show that a local minima is always appeared outside of the ISCO for $1 < a_* < 1.1$ in Ω_θ curves, in principle. This feature is completely absent in the case of a BH.

shows that the observed LF QPOs could be identified with Ω_{nod} only for $a_* < 0.5$ and $a_* \sim 1.089$ (see also [33]). In fact, Ω_{nod} could have a much higher value for a_* closer to 1 for both BH and NS, and it could be possible to identify an HF QPO with Ω_{nod} (Table I). If a_* is very close to 1, Ω_{nod} value is quite high (Table I), and such high frequency QPOs could be detected in future for BH and NS with $a_* \approx 1$. While there are uncertainties in the specific identifications of observed frequencies with the theoretical ones, the recent discovery of the C-type quasi-periodic variation of the broad relativistic iron line energy from the BHXB H1743–322 strongly suggests that the inner accretion disk of this source is indeed tilted and precessing [34]. Therefore, the theoretical dependencies of various frequencies on a_* , as discussed in this section, have potential to distinguish between a BH and a NS.

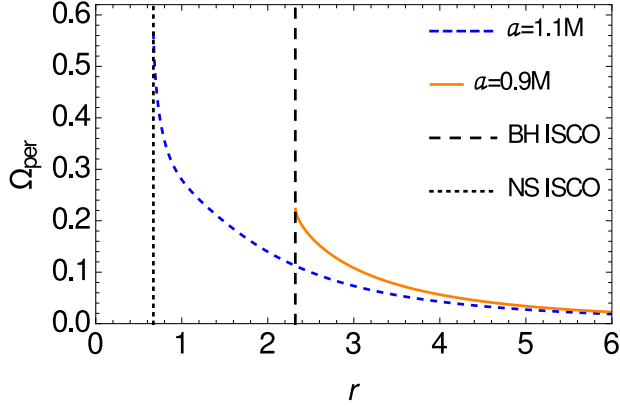


FIG. 15. Comparison between the periastron precession frequencies (Ω_{per} in units of M^{-1}) of a BH and a NS at their respective ISCOs for $\epsilon = \pm 0.1$. BH ISCO and NS ISCO are located at $2.32 M$ and $0.67 M$ respectively.

How could this be done? Here we give some examples. Note that most of the BHXBs are transient sources, and an accretion disk is formed only during an outburst. Even for the persistent BHXBs, source state often changes, which implies changes in accretion components. So it is expected that the accretion disk of a given BHXB sometimes advances towards the central object, and sometimes recedes, depending on the source intensity and spectral states. If QPOs are connected to the natural frequencies mentioned above, then such a dynamics of the disk would mean changes in QPO frequencies, as these frequencies depend on the radial distance. And we do observe evolution of QPO frequencies. As a BH and a NS have significantly different theoretical radial profiles of frequencies, it could be, in principle, possible to distinguish them by tracking the evolution of QPO frequencies as the disk advances or recedes. For example, Ω_{nod} for a BH will monotonically increase, and will attain the maximum value, if the disk advances up to the ISCO radius. But Ω_{nod} for a NS will first increase, will attain the maximum value, and then will decrease, as the disk advances up to r_{ISCO} , which can be quite different from the r_{ISCO} of BHs. In fact, in case of a NS, the absolute value of Ω_{nod} can become zero and then increase again. Whether this will happen, and radial locations of the maximum and zero values of Ω_{nod} depend on a_* . Therefore, the Lense-Thirring precession can provide a way to distinguish between a BH and a NS. Similarly, the maximum possible value of Ω_ϕ depends on a_* . Finally, according to the above mentioned model, Ω_r is interpreted as the separation between two HF QPO frequencies. Therefore, the qualitatively different Ω_r radial profiles for NSs with $a_* \lesssim 1.05$ can be useful to distinguish them from BHs.

VIII. CONCLUSION

The spin precession frequency of test gyros, in the BH case, are finite inside and outside of the ergoregion but diverge as one considers a gyro close to the horizon, $r \sim r_+$, for any direction ($0 < \theta \leq \pi/2$). This feature can also help us to detect the horizon of a BH. In case of the NS, spin precession frequency of gyros remain finite and regular even if one considers gyros close to $r = 0$, for all θ in the range: $0 < \theta < \pi/2$, with a suitable value of Ω_e . Maxima/minima in the radial profile of the precession frequency (for eg., two local maxima or two local minima or two peaks or three peaks with a plateau) would indicate a ‘near-extremal NS’ with ($a_* < 1.1$) since such features are completely absent in a BH or a NS with higher angular momentum ($a_* \geq 1.1$).

In case of the nodal plane precession, related to the accretion disc, we can summarize here the distinctive features of the LT frequency in both BH and NS spacetimes, using which one can make a conclusive statement regarding the existence of a NS:

- (i) We obtain a peak value of Ω_{nod} at $r_p(a_*)$ for all $a_* > 1$.
- (ii) Ω_{nod} vanishes in a particular orbit of radius r_0 for $a_* \geq 1.089$.
- (iii) Ω_{nod} becomes negative (which means that the LT precession reverses direction) in all the orbits which are in the range $r_0 > r \geq r_{\text{ISCO}}$ for $a_* > 1.089$.
- (iv) Additionally, Ω_{nod} shows an ‘adverse’ effect : $\Omega_{\text{nod}} \propto r^n$ (where $n \gtrsim 0$, see FIG.10) in the region $r_0 \leq r < r_p$. This curve does not follow the inverse cube law of distance like other astrophysical objects. All these features are completely absent in the case of BH and this would be reflected in the observation of frequencies of QPOs.

Finally, it can be seen from FIG.13 and FIG.14 that Ω_r and Ω_θ also have some characteristic differences in the cases of BH and NS by which it may be possible to detect a NS if Ω_r and Ω_θ are the observationally measurable quantities.

-
- [1] <http://www.eventhorizontelescope.org/>
 - [2] C. Chakraborty, P. Majumdar, *Class. Quantum Grav.* **31**, 075006 (2014)
 - [3] C. Chakraborty, P. Kocherlakota, P. S. Joshi, arXiv:1605.00600v2 [gr-qc], (2016)
 - [4] P. S. Joshi, D. Malafarina, R. Narayan *Class. Quantum Grav.* **31**, 015002 (2014)
 - [5] D. Bini, A. Geralico, R. T. Jantzen, *Phys. Rev. D* **94**, 064066 (2016)
 - [6] D. Bini, A. Geralico, R. T. Jantzen, arXiv:1610.06513 [gr-qc] (2016)

- [7] S. A. Hojman, F. A. Asenjo, *Class. Quantum Grav.* **30**, 025008 (2013)
- [8] C. Armaza, M. Banados, B. Koch, *Class. Quantum Grav.* **33**, 105014 (2016)
- [9] N. Straumann, *General Relativity with applications to Astrophysics*, Springer (2009)
- [10] C. Chakraborty, K. P. Modak, D. Bandyopadhyay, *ApJ* **790**, 2 (2014)
- [11] E. G. Gimon, P. Horava, *Phys. Lett. B* **672**, 299 (2009)
- [12] J. B. Hartle, *Gravity: An introduction to Einstein's General relativity*, Pearson (2009)
- [13] K. Sakina, J. Chiba, *Phys. Rev. D* **19**, 2280 (1979)
- [14] M. Patil, P.S. Joshi, *Class. Quantum Grav.* **28**, 235012 (2011)
- [15] M. Patil, P.S. Joshi, *Phys. Rev. D* **84**, 104001 (2011)
- [16] M. Banados, J. Silk, S. West, *Phys. Rev. Lett.* **103**, 111102 (2009)
- [17] T. Harada and M. Kimura *Class. Quantum Grav.* **31** 243001 (2014)
- [18] M. Patil, T. Harada, K. Nakao, P.S. Joshi, M. Kimura *Phys. Rev. D* **93**, 104015 (2016)
- [19] J. Schnittman, *Phys. Rev. Lett.* **113** 261102, (2014)
- [20] A. T. Okazaki, S. Kato, J. Fukue, *PASJ* **39**, 457 (1987)
- [21] S. Kato, *PASJ* **42**, 99 (1990).
- [22] J. Lense, H. Thirring, *Phys. Z.* **19**, 156-163, (1918)
- [23] T. M. Belloni, L. Stella, *Space Sci Rev* **183**, 43, (2014)
- [24] J. M. Bardeen, W. H. Press, S. A. Teukolsky, *ApJ* **178**, 347 (1972)
- [25] D. Pugliese, H. Quevedo, R. Ruffini, *PRD* **84**, 044030 (2011)
- [26] S. Chandrasekhar, *The Mathematical Theory of Black Holes*, Oxford (1992)
- [27] T. M. Belloni, L. Stella, *Space Science Reviews* **183**, 43 (2014)
- [28] T. Belloni, A. Sanna, M. Méndez, *MNRAS* **426**, 1701 (2012)
- [29] L. Stella, M. Vietri, *ApJ* **492**, L59 (1998)
- [30] L. Stella, M. Vietri, *Phys. Rev. Lett.* **503**, 350 (1999)
- [31] A. Ingram, S. Motta, *MNRAS* **444**, 2065 (2014)
- [32] S. Motta et al., *MNRAS* **437**, 2554 (2014) ; S. Motta et al., *MNRAS* **439**, d5 (2014)
- [33] L. Stella, A. Possenti, *Space Sci. Rev.* **148**, 105 (2009)
- [34] A. Ingram et. al, *MNRAS* **461**, 1967 (2016)